

# 15 Cosmological Physics

*Hu Zhan, Asantha Cooray, Salman Habib, Alan F. Heavens, Anthony Tyson, Licia Verde, Risa H. Wechsler*

The ultimate goal of astronomical surveys is to deepen our fundamental understanding of the Universe. One specific question to be addressed is the cosmological framework within which we interpret the observations. Because it is not feasible to physically perturb the Universe for investigation, cross checks and confirmations by multiple lines of evidence are extremely important in cosmology. The acceptance of dark matter by the community nearly 50 years after the seminal proposal of Zwicky (1933, 1937) is a perfect example of how observations of galaxy rotational curves (e.g., Rubin, Thonnard, & Ford 1978), dynamics of galaxy groups and clusters (for a review, see Faber & Gallagher 1979), and galaxy X-ray emission (e.g., Fabricant, Lecar, & Gorenstein 1980) from various surveys, working in unison, eventually shifted our paradigm of the Universe.

The accelerated cosmic expansion, inferred from luminosity distances of type Ia supernovae (Riess et al. 1998; Perlmutter et al. 1999) and reinforced by large-scale structure and CMB observations (Spergel et al. 2003) has led to yet another puzzle – dark energy. It poses a challenge of such magnitude that, as stated by the Dark Energy Task Force (DETF), “nothing short of a revolution in our understanding of fundamental physics will be required to achieve a full understanding of the cosmic acceleration” (Albrecht et al. 2006).

The lack of multiple complementary precision observations is a major obstacle in developing lines of attack for dark energy theory. This lack is precisely what LSST will address via the powerful techniques of weak lensing (WL, Chapter 14) and baryon acoustic oscillations (BAO, Chapter 13) – galaxy correlations more generally – in addition to SNe (Chapter 11), cluster counts (§ 13.6), and other probes of geometry and growth of structure (such as  $H_0$  from strong lensing time delay measurements in § 12.4). The ability to produce large, uniform data sets with high quality for multiple techniques is a crucial advantage of LSST. It enables not only cross checks of the result from each technique but also detections of unknown systematics and cross-calibrations of known systematics. Consequently, one can achieve far more robust and tighter constraints on cosmological parameters and confidently explore the physics of the Universe beyond what we know now.

Because the observables of these probes are extracted from the same cosmic volume, correlations between different techniques can be significant. New observables can also emerge, e.g., galaxy-shear correlations. A joint analysis of all the techniques with LSST must involve careful investigations of the cross-correlations between these techniques.

In this Chapter, we describe several cosmological investigations enabled by the combination of various LSST and external data sets. § 15.1 mainly demonstrates the complementarity between BAO (galaxy angular power spectra, § 13.3) and WL (shear power spectra, § 14.4) techniques in constraining the dark energy equation of state (EOS), especially in the presence of systematic

uncertainties. Results from LSST SNeIa and cluster counts are shown at the end of this section. Density fluctuations measured by BAO and WL are sensitive to the sum of the neutrino masses. We estimate in § 15.2 that LSST, in combination with Planck, can constrain the neutrino mass to  $\Delta m_\nu < 0.1$  eV and determine the mass hierarchy. Conventional dark energy affects the growth of structure indirectly through the expansion background, i.e., the Hubble “drag,” assuming that dark energy clusters occur only on very large scales and with small amplitude. In contrast, gravity that deviates from General Relativity (“modified gravity”) can have a direct impact on clustering at all scales. Because the probes mentioned above and in previous chapters are sensitive to both the expansion history of the Universe and the growth of structures, LSST can place useful constraints on gravity theories as well. Several examples are given in § 15.3. § 15.4 shows that LSST can take the advantage of being a very wide and deep survey to test the isotropy of distance measurements across the sky and constrain anisotropic dark energy models. We finish with a discussion of requirements on the cosmological simulations needed for carrying out the analyses described in this and previous chapters. The details of the statistical analyses are given in Appendix B.

## 15.1 Joint Analysis of Baryon Oscillations and Weak Lensing<sup>1</sup>

*Hu Zhan*

### 15.1.1 Introduction

BAO (galaxy power spectra, § 13.3) and WL (shear power spectra, § 14.4) techniques each have their own systematics and parameter degeneracies. When the shear and galaxy distribution are analyzed jointly, one gains from the extra information in the galaxy–shear cross power spectra, which is not captured in either technique alone. Moreover, the two techniques can mutually calibrate some of their systematics and greatly strengthen parameter constraints.

The WL technique extracts cosmological information from the distribution of minute distortions (shear) to background galaxies caused by foreground mass (see § 14.1). It has the advantage that it measures the effect of all matter, luminous or not, so that the shear statistics reflect the clustering properties of the bulk of the matter – dark matter, for which gravity alone can provide fairly robust predictions via linear theory on large scales and  $N$ -body simulations on small scales. To achieve its power, however, the WL technique requires unprecedented control of various systematic effects. One example is the photometric redshift error distribution. Because the kernel of the WL shear power spectrum peaks broadly between the observer and the source, the shear power spectrum is not very sensitive to the redshift distribution of source galaxies. For a redshift bin at  $z = 2$ , a shift of the bin by  $\Delta z = 0.1$  causes very little change in the shear power spectrum. However, the inference for cosmological parameters can change more markedly with the redshift difference  $\Delta z = 0.1$ . In other words, one must know the true-redshift distribution of galaxies in each photometric redshift bin accurately in order to interpret the WL data correctly.

---

<sup>1</sup>Weak lensing in this section refers to two-point shear tomography (§ 14.4.1) only. In the joint analysis of baryon oscillations and weak lensing, galaxy–shear cross power spectra (§ 14.2) are also included.

Galaxies provide a proxy for mass. One may relate fluctuations in the galaxy number density to those in all matter by the galaxy clustering bias, which evolves with time and is assumed to be scale independent only on large scales. Although this does not severely impact the BAO technique, which utilizes the small oscillatory features in the galaxy power spectrum to measure distances (see § 13.3), knowing the galaxy bias accurately to the percent level does help improve cosmological constraints from BAO. Because the kernel of the galaxy (angular) power spectrum is determined by the true-redshift distribution of galaxies in a photometric redshift bin, galaxy power spectra can be sensitive to the photometric redshift error distribution. For instance, with the Limber approximation, the cross power spectrum between two redshift bins is given by the overlap between the two bins in true-redshift space. A small shift to one of the redshift bins can change the amplitude of the cross power spectrum significantly, suggesting that the galaxy power spectra can help calibrate the photometric redshift error distribution (§ 14.5.1).

### 15.1.2 Galaxy and Shear Power Spectra

We extend the definition of galaxy power spectrum in § 13.3 and shear power spectrum in § 14.4 to include the galaxy–shear power spectrum (Hu & Jain 2004; Zhan 2006)

$$P_{ij}^{XY}(\ell) = \frac{2\pi^2\ell}{c} \int_0^\infty dz H(z) D_A(z) W_i^X(z) W_j^Y(z) \Delta_\phi^2(k; z), \quad (15.1)$$

where lower case subscripts correspond to the tomographic bins, upper case superscripts label the observables, i.e.,  $X = g$  for galaxies or  $\gamma$  for shear;  $H(z)$  is the Hubble parameter,  $D_A(z)$  is the comoving angular diameter distance,  $\Delta_\phi^2(k; z)$  is the dimensionless power spectrum of the potential fluctuations of the density field, and  $k = \ell/D_A(z)$ . BAO and WL do not necessarily use the same binning. In other words, the bin number is defined for each technique separately. The window function is

$$W_i^X(z) = \begin{cases} \frac{n_i(z)}{\bar{n}_i} \frac{2ab(z)}{3\Omega_m H_0^2 D_A^2(z)} & X = g \\ \frac{1}{cH(z)D_A(z)} \int_z^\infty dz' \frac{n_i(z')}{\bar{n}_i} \frac{D_A(z, z')}{D_A(z')} & X = \gamma, \end{cases} \quad (15.2)$$

where  $b(z)$  is the linear galaxy clustering bias, and  $\Omega_m$  and  $H_0$  are, respectively, the matter fraction at  $z = 0$  and Hubble constant. The galaxy redshift distribution,  $n_i(z)$ , in the  $i$ th tomographic bin is an average of the underlying three-dimensional galaxy distribution over angles, and the mean surface density,  $\bar{n}_i$ , is the total number of galaxies per steradian in bin  $i$ . The distribution,  $n_i(z)$ , is broader than the nominal width of the tomographic bin (defined in photometric redshift space) because of photometric redshift errors.

We only include galaxy power spectra on largely linear scales, e.g., the scales of BAOs, in our analysis, so that we can map the matter power spectrum to galaxy power spectrum with a scale-independent but time-evolving linear galaxy bias (Verde et al. 2002; Tegmark et al. 2004). One may extend the analysis to smaller scales with a halo model to describe the scale dependency of the galaxy bias and, in fact, can still constrain the scale-dependent galaxy bias to 1% level (Hu & Jain 2004).

The observed power spectra have contributions from galaxy shot (shape) noise  $\bar{n}_i^{-1}$  ( $\gamma_{\text{rms}}^2 \bar{n}_i^{-1}$ ), multiplicative errors  $f_i^X$ , and additive errors  $A_i^X$ :

$$(C_\ell^{XY})_{ij} = (1 + \delta_{X\gamma}^K f_i^X + \delta_{Y\gamma}^K f_j^Y) P_{ij}^{XY}(\ell) + \delta_{XY}^K \left[ \delta_{ij}^K \frac{X_{\text{rms}}^2}{\bar{n}_i} + \rho_{ij}^X A_i^X A_j^Y \left( \frac{\ell}{\ell_*^X} \right)^{\eta^X} \right], \quad (15.3)$$

where  $\delta_{XY}^K$  and  $\delta_{ij}^K$  are Kronecker delta functions,  $\rho_{ij}^X$  determines how strongly the additive errors of two different bins are correlated, and  $\eta^X$  and  $\ell_*^X$  account for the scale dependence of the additive errors. Again,  $X$  and  $Y$  refer to galaxies  $g$  or shear  $\gamma$ . For galaxies,  $g_{\text{rms}} \equiv 1$ , and, for the shear,  $\gamma_{\text{rms}} \sim 0.2$  is due to the intrinsic shape of galaxies and measurement errors. Note that the multiplicative error of galaxy number density is degenerate with the galaxy clustering bias and is hence absorbed by  $b_i$ . Below the levels of systematics future surveys aim to achieve, the most important aspect of the (shear) additive error is its amplitude (Huterer et al. 2006), so we simply fix  $\rho^X = 1$  and  $\eta^X = 0$ . For more comprehensive accounts of the above systematic uncertainties, see Huterer et al. (2006), Jain et al. (2006), Ma et al. (2006), and Zhan (2006).

We forecast LSST performace with a Fisher matrix analysis. See § B.4.2 for a detailed description of the Fisher matrix calculation. The BAO aspect of the calculations, which includes the galaxy binning, galaxy bias, and photometric redshift treatment, is the same as that in § 13.3. WL results in this section are based on the two-point shear tomography described in § 14.4, and the joint BAO and WL results include the galaxy–shear power spectra (Equation 15.3) as well. We use 10 shear bins evenly spaced between  $z = 0.001$  and 3.5.

### 15.1.3 Complementarity Between BAO and WL

BAO and WL have their unique strengths and are very complementary to each other. A joint analysis benefits from the strength of each technique: BAO can help self-calibrate the photometric redshift error distribution, while WL can help constrain the galaxy bias as the different power spectra have different dependence on the galaxy bias.

Photometric redshift errors are one of the most critical systematics for WL tomography. Redshift errors directly affect the interpretation of the distance–redshift and growth–redshift relations. Because of its broad lensing kernel, WL cannot self-calibrate the photometric redshift error distribution, but, as shown in § 13.3, the cross-bin galaxy power spectra can calibrate the photometric redshift rms and bias parameters to  $\sim 10^{-3}(1+z)$ , which is sufficient for WL (Ma et al. 2006; Zhan 2006).

Figure 15.1 demonstrates that while the WL constraints on the dark energy EOS parameters,  $w_0$  and  $w_a$ , are sensitive to systematic uncertainties in the photometric redshift error distribution, the joint BAO and WL results remain fairly immune to these systematics. The dramatic improvement of the BAO+WL results over the WL-alone results is due to the cross-calibration of galaxy bias and photometric redshift uncertainties and is independent of the dark energy EOS parametrization.

The statistics-only results in Figure 15.1 are marginalized over the other nine cosmological parameters listed in Table A.1 and 30 galaxy clustering bias parameters. We impose no prior on the galaxy bias (for numerical reasons, we take  $\sigma_P(\ln b_i) = 1000$ ). The photometric redshift parameters are fixed, and the power spectra errors in Equation 15.3 are not included.

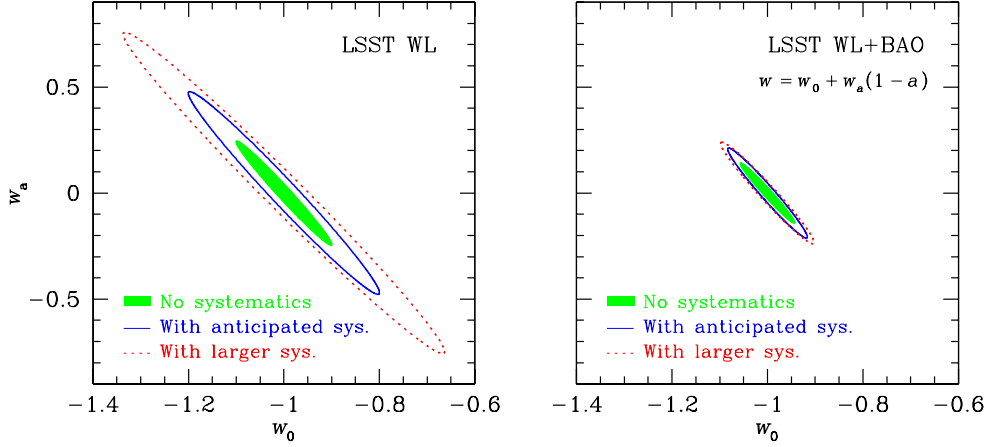


Figure 15.1:  $1\text{-}\sigma$  error contours of the dark energy EOS parameters  $w_0$  and  $w_a$  from LSST WL shear power spectra (left panel) and joint LSST WL and BAO (right panel). The shaded areas represent the results with statistical errors only. The solid contours correspond to those with the anticipated level of systematic errors, which include the uncertainty in the photometric redshift error distribution and additive and multiplicative errors in the power spectra (see, e.g., § 3.8 and § 14.5). The assumed photometric redshift systematics would require a redshift calibration sample of 3000 spectra per unit redshift interval if the photometric redshift error distribution were Gaussian. The dotted contours relax the requirement to 188 spectra per unit redshift. A much larger sample will be needed for realistic photometric redshifts. The joint WL and BAO results are less affected by the systematics because of the ability to self-calibrate the systematics. See text for details of the calculations.

For anticipated systematics, we assume that  $\sigma_P(\delta z_i) = 2^{-1/2}\sigma_P(\sigma_{z,i}) = 0.05\sigma_{z,i} = 0.0025(1+z)$ ,  $\sigma_P(f_i) = 0.005$ ,  $A_i^g = 10^{-4}$ , and  $A_i^\gamma = 10^{-5}$ . For larger systematics, we relax the photometric redshift priors to  $\sigma_P(\delta z_i) = 2^{-1/2}\sigma_P(\sigma_{z,i}) = 0.2\sigma_{z,i} = 0.01(1+z)$  and  $A_i^\gamma = 10^{-4.5}$ . See § 3.8 and § 14.5 for discussions about the systematics.

The linear galaxy clustering bias,  $b$ , is degenerate with the linear growth function,  $G$ , for the angular BAO technique. Therefore, one cannot extract much useful information from the growth of the large-scale structure with photometric redshift BAO. One can break this degeneracy by jointly analyzing the galaxy and shear power spectra, because the galaxy–galaxy, galaxy–shear, and shear–shear power spectra depend on different powers of the linear galaxy bias ( $b^2$ ,  $b^1$ , and  $b^0$  respectively). CMB data help as well by providing an accurate normalization of the matter power spectrum. The resulting constraints on the linear galaxy bias parameters can reach the percent level (Hu & Jain 2004; Zhan 2006; Zhan, Knox, & Tyson 2009), so that growth information can be recovered from galaxy power spectra as well.

#### 15.1.4 Precision Measurements of Distance and Growth Factor

Dark energy properties are derived from variants of the distance–redshift and growth–redshift relations. Different dark energy models feature different parameters, and various phenomenological parametrizations may be used for the same quantity such as the EOS. In contrast, distance and growth measurements are model-independent, as long as dark energy does not alter the matter power spectrum directly. Hence, it is desirable for future surveys to provide results of the distance

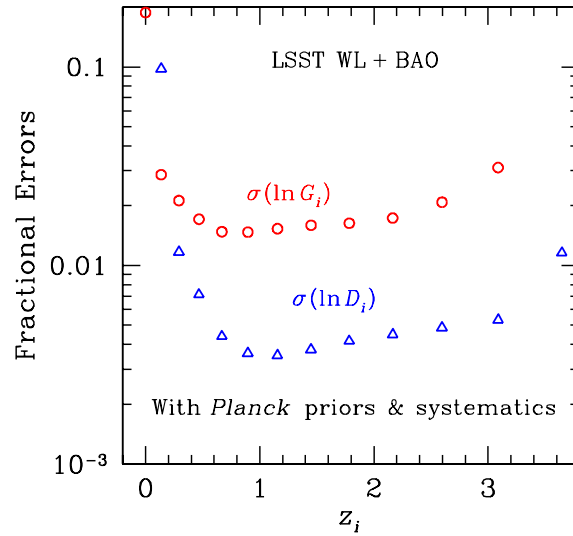


Figure 15.2: Marginalized  $1\sigma$  errors on the co-moving distance (open triangles) and growth factor (open circles) parameters from the joint analysis of LSST BAO and WL (galaxy–galaxy, galaxy–shear, and shear–shear power spectra) with a conservative level of systematic uncertainties in the photometric redshift error distribution and additive and multiplicative errors in the shear and galaxy power spectra. The maximum multiple used for WL is 2000, and that for BAO is 3000 (with the additional requirement  $\Delta_\delta^2(\ell/D_A; z) < 0.4$ ). The growth parameters,  $G_0 \dots D_{14}$ , are evenly spaced in  $\log(1+z)$  between  $z = 0$  and 5, and the distance parameters,  $D_1 \dots D_{14}$ , start at  $z_1 = 0.14$  (see text for details). The error of each distance (growth) parameter is marginalized over all the other parameters including growth (distance) parameters and other distance (growth) parameters. The joint constraints on distance are relatively insensitive to the assumed systematics. Figure from Zhan et al. (2009), with permission.

and growth of structure, so that different theoretical models can be easily and uniformly confronted with the data.

Figure 15.2 demonstrates that joint LSST BAO and WL can achieve  $\sim 0.5\%$  precision on the distance and  $\sim 2\%$  on the growth factor from  $z = 0.5$  to 3 in each interval of  $\Delta z \sim 0.3$  (Zhan et al. 2009). Such measurements can test the consistency of dark energy or modified gravity models (e.g., Knox 2006; Heavens et al. 2007).

### 15.1.5 Constraining the Mean Curvature

The mean curvature of the Universe has a significant impact on dark energy measurements. For example, the curvature parameter  $\Omega_k$  is completely degenerate with a  $w = -1/3$  dark energy if dark energy clustering (§ 13.7) is neglected. In the concordance  $\Lambda$ CDM model ( $w = -1$ ), allowing  $\Omega_k$  to float greatly weakens the ability of supernovae at  $z < 1.7$  to constrain  $w_a$  (Linder 2005b; Knox 2006). LSST BAO and WL can determine  $\Omega_k$  to  $\sim 10^{-3}$  separately and  $< 10^{-3}$  jointly, and their results on  $w_0$  and  $w_a$  are not affected in practice by the freedom of  $\Omega_k$  (Zhan 2006; Knox 2006). The reason is that low-redshift growth factors, which can be measured well by WL, and high-redshift distances, which can be measured well by BAO, are very effective for measuring  $\Omega_k$  and, hence, lifting the degeneracy between  $\Omega_k$  and  $w_a$  (Zhan & Knox 2006). Given its large area, LSST can place a tight upper limit on curvature fluctuations, which are expected to be small ( $\sim 10^{-5}$ ) at the horizon scale in standard inflation models.

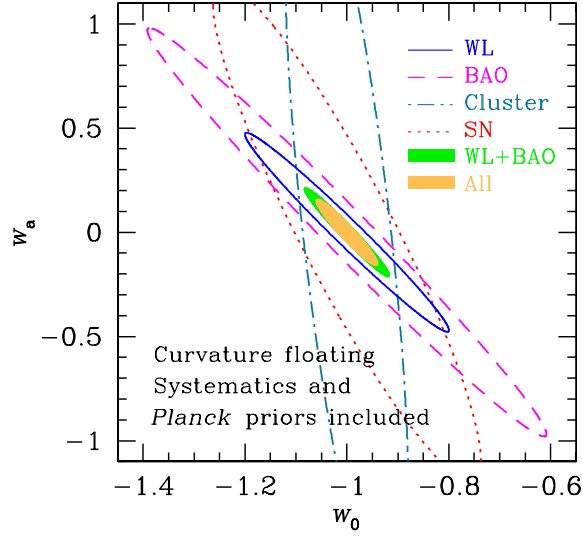


Figure 15.3: Joint  $w_0$ – $w_a$  constraints from LSST BAO (dashed line), cluster counting (dash-dotted line), supernovae (dotted line), WL (solid line), joint BAO and WL (green shaded area), and all combined (yellow shaded area). The BAO and WL results are based on galaxy–galaxy, galaxy–shear, and shear–shear power spectra only. Adding other probes such as strong lensing time delay (§ 12.4), ISW effect (§ 13.7), and higher-order galaxy and shear statistics (§ 13.5 and § 14.4) will further improve the constraints.

The aforementioned results are obtained either with the assumption of matter dominance at  $z \gtrsim 2$  and precise independent distance measurements at  $z \gtrsim 2$  and at recombination (Knox 2006) or with a specific dark energy EOS:  $w(z) = w_0 + w_a z(1+z)^{-1}$  (Knox et al. 2006b; Zhan 2006). However, if one assumes only the Robertson-Walker metric without invoking the dependence of the co-moving distance on cosmology, then the pure metric constraint on curvature from a simple combination of BAO and WL becomes much weaker:  $\sigma(\Omega'_k) \simeq 0.04 f_{\text{sky}}^{-1/2} (\sigma_{z0}/0.04)^{1/2}$  (Bernstein 2006)<sup>2</sup>.

Our result for  $\Omega'_k$  from LSST WL or BAO alone is not meaningful, in agreement with Bernstein (2006). However, because WL and BAO measure very different combinations of distances (see, e.g., Figure 6 of Zhan et al. 2009), breaking the degeneracy between  $\Omega'_k$  and other parameters, the joint analysis of the two leads to  $\sigma(\Omega'_k) = 0.017$ , including anticipated systematics in photometric redshifts and power spectra for LSST. This result is better than the forecast derived from the shear power spectra and galaxy power spectra in Bernstein (2006) because we include in our analysis more information: the galaxy–shear power spectra.

### 15.1.6 Results of Combining BAO, Cluster Counting, Supernovae, and WL

We show in Figure 15.3  $w_0$ – $w_a$  constraints combining four LSST probes of dark energy: BAO, cluster counting, supernovae, and WL. The cluster counting result is from Fang & Haiman (2007) and the supernova result is based on Zhan et al. (2008). Because each probe has its own parameter degeneracies, the combination of any two of them can improve the result significantly. As mentioned

<sup>2</sup> $\Omega_k$  affects both the co-moving distance and the mapping between the co-moving distance and the angular diameter distance, while  $\Omega'_k$  affects only the latter. See Equation 13.12.

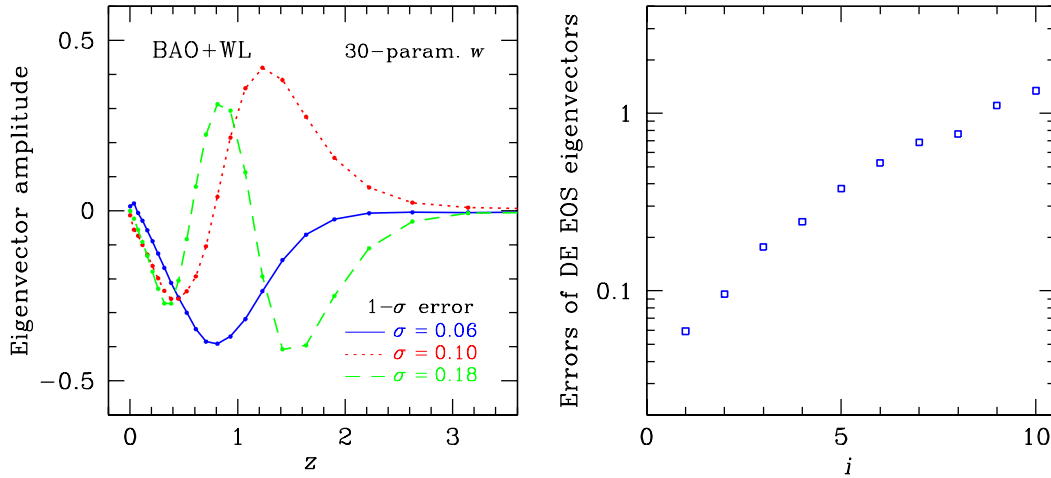


Figure 15.4: Eigensystem analysis of joint LSST BAO and WL (galaxy–galaxy, galaxy–shear, and shear–shear power spectra) constraints on a 30-dimensional dark energy EOS model. The dark energy EOS is spline-interpolated between 30 EOS parameters evenly spaced between  $a = 0$  and 1 with a fiducial model of  $w = -1$ . *Left panel:* The first three best-determined dark energy EOS eigenmodes (departure from  $w = -1$ ) with LSST BAO+WL. *Right panel:*  $1-\sigma$  errors of the EOS eigenmodes. The errors will be proportional to the square root of the dimension of the dark energy EOS for sufficiently large dimensions.

above, BAO and WL are highly complementary to each other. Much of the complementarity is actually in parameter space (such as photometric redshifts and galaxy bias) that has been marginalized over. In Figure 15.3, we see that cluster counting is quite effective in constraining  $w_0$  and that it is directly complementary to WL and BAO in the  $w_0-w_a$  plane. When all the four probes are combined, the error ellipse area decreases by  $\sim 30\%$  over the joint BAO and WL result.

The  $w_0-w_a$  parametrization in Figure 15.3 does not capture the complexity of all dark energy models. It also significantly underestimates the full capabilities of Stage 4 surveys (Albrecht & Bernstein 2007), such as that of the LSST. More generally, one may allow the EOS to vary independently at different redshifts and let the data determine the EOS eigenmodes and their errors, which can then be used to constrain dark energy models. Figure 15.4 presents the best determined dark energy EOS eigenmodes and their errors from LSST BAO+WL for a 30-dimensional EOS model (Albrecht & Bernstein 2007; Albrecht et al. 2009). It is seen that the best determined mode is sensitive to the dark energy EOS at  $z \sim 0.8$ . The eigensystem analysis gives the expected noise of the eigenmodes, and one can then project dark energy models into the orthogonal eigenmode space to constrain the models. Detailed calculations show that LSST can eliminate a large space of quintessence models (e.g., Barnard et al. 2008).

## 15.2 Measurement of the Sum of the Neutrino Mass

*Licia Verde, Alan F. Heavens*

Current limits on the neutrino mass from cosmology come most robustly from the CMB,  $\sum m_\nu < 1.3$  eV at 95% confidence (Dunkley et al. 2009), and with the addition of large-scale structure and supernova data to  $< 0.6$  eV (Komatsu et al. 2009). With the addition of Lyman  $\alpha$  data, the

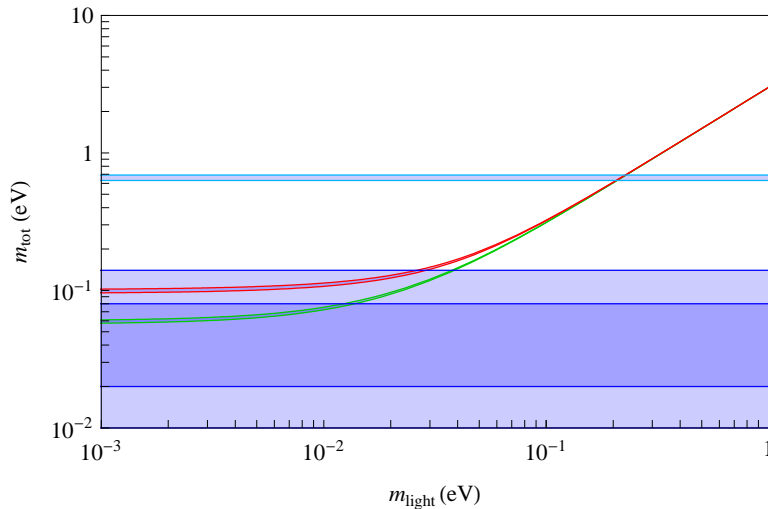


Figure 15.5: Forecasted constraints in the context of what is known to date from neutrino oscillations experiments. The x-axis is the mass of the lightest neutrino in eV, and the y-axis is the sum of neutrino masses (also in eV). The narrow green band represents the normal hierarchy and the narrow red band the inverted one: for light neutrinos the two hierarchies are in principle distinguishable. The light blue (horizontal shaded) regions represent the  $1 - \sigma$  constraints for the combination Planck+LSST three-dimensional lensing, for two fiducial models of massive and nearly massless lightest neutrino, consistent with the normal hierarchy. The lighter regions are  $1 - \sigma$  constraints for a general cosmological model with massive neutrinos (see text for details). The darker horizontal band shows the forecasted  $1 - \sigma$  constraint obtained in the context of a power-law  $P(k)$ ,  $\Lambda$ CDM + massive neutrinos model. These constraints offer the possibility in principle to distinguish between the normal and inverted hierarchies. Figure courtesy of E. Fernandez-Martinez.

limits may be pushed as low as 0.17 eV (Seljak et al. 2006), with model-dependent assumptions. For a summary of experimental limits on neutrino masses, see Fogli et al. (2008). In the future, the primary robust tools for constraining massive neutrinos are the CMB combined with a large scale structure survey and measurement of the three-dimensional cosmic shear. In the three-dimensional cosmic shear technique (Heavens 2003; Castro et al. 2005; Heavens et al. 2006; Kitching et al. 2007) the full three-dimensional shear field is used without redshift binning, maximizing the information extracted. Massive neutrinos suppress the growth of the matter power spectrum in a scale-dependent way, and it is from this signature that cosmic shear measurements can constrain neutrino properties. Inevitably, there is a degeneracy with dark energy parameters, as dark energy also affects the growth of perturbations (Kiakotou et al. 2008). Following Kitching et al. (2008a) we explore the constraints on neutrino properties obtained with a Fisher matrix approach for a survey with the characteristics of LSST assuming a Planck prior. Unless otherwise stated, the reported constraints are obtained allowing for running of the spectral index of the primordial power spectrum, non-zero curvature and for a dark energy component with equation of state parametrization given by  $w_0, w_a$ ; all results on individual parameters are fully marginalized over all other cosmological parameters.

By combining three-dimensional cosmic shear constraints achievable with a survey like LSST with constraints achievable with Planck's data, the massive neutrino (fiducial values  $m_\nu = 0.66$  eV ;  $N_\nu = 3$ ) parameters could be measured with marginal errors of  $\Delta m_\nu \sim 0.03$  eV and  $\Delta N_\nu \sim 0.08$ , a factor of 4 improvement over Planck alone. If neutrinos are massless or have a very small mass

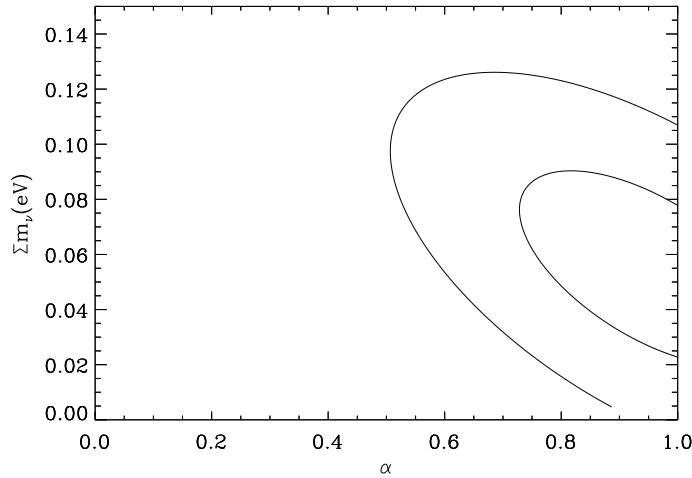


Figure 15.6: The 68% and 95% confidence intervals for the sum of neutrino masses and the fraction of mass in the heaviest neutrino, using Planck and LSST’s WL survey, marginalized over other parameters in a 10-parameter cosmological model. Figure from [De Bernardis et al. \(2009\)](#), with permission.

(fiducial model  $m_\nu = 0$  eV ;  $N_\nu = 3$ ) the marginal errors on these parameters degrade ( $\Delta m_\nu \sim 0.07$  eV and  $\Delta N_\nu \sim 0.1$ ), but there is still a similar improvement over Planck alone. This degradation in the marginal error occurs because the effect of massive neutrinos on the matter power spectrum and hence on three-dimensional weak lensing is non-linear. These findings are in good agreement with an independent analysis ([Hannestad et al. 2006](#)). Alternatively, the constraints could improve by as much as a factor of 2 if complementary data sets (such as direct measurements of the expansion history from BAO or supernovae) were used to lift the degeneracies between  $m_\nu$  and the running of the spectral index,  $w_a$  and  $w_0$  ([Kitching, private communication](#)). As discussed in [Kitching et al. \(2008b\)](#) and [Kitching et al. \(2008a\)](#), a degradation in errors by a factor of  $\sim \sqrt{2}$  is expected due to systematics.

[Figure 15.5](#) shows these constraints in the context of what is known currently from neutrino oscillations experiments. Particle physics shows that neutrinos come in three flavors: muon, tau, and electron neutrinos and that they oscillate i.e., as they propagate they can change flavor; the neutrino flavor eigenstates are not the same as the neutrino mass eigenstates (simply called 1 2 3). In the standard model for particle physics, the existence of flavor oscillations implies a non-zero neutrino mass because the amount of mixing between the flavors depend on their mass differences. The properties of the mixing are described by a “mixing matrix” which is like a rotation matrix specified by the mixing angles  $\theta_{12}$ ,  $\theta_{13}$ , etc. Oscillation experiments have so far determined absolute values of neutrino mass differences, one mass difference being much smaller than the other one. However neither the sign of the mass difference nor the absolute mass scale are known. There are, therefore, two possibilities: a) the “normal hierarchy,” two neutrinos are much lighter than the third or b) an “inverted hierarchy,” in which one neutrino is much lighter than the other two. Cosmology, being sensitive to the sum of the neutrino masses, can offer complementary information to particle physics experiments in two ways: a) a determination of the total neutrino mass will give an absolute mass scale and b) since in the normal hierarchy the sum of neutrino masses is lower (by up to a factor of 2, depending on the absolute mass scale) than in the inverted hierarchy, a determination of the total neutrino mass with an error  $\ll 0.1$  eV may select the neutrino hierarchy.

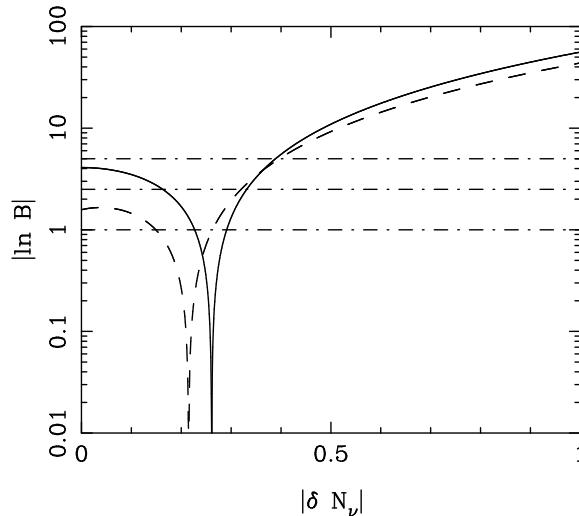


Figure 15.7: The predicted evidence for the number  $N_\nu$  of neutrinos individually for three-dimensional cosmic shear using the fiducial survey combined with a Planck prior. The solid line shows the conditional evidence assuming that the other parameter is fixed at its fiducial value, the dashed line shows the marginal expected evidence when the possible values of the hidden parameter are taken into account. The dot-dashed lines show the defining evidence limits on the Jeffreys scale where  $\ln B < 1$  is “inconclusive,”  $1 < \ln B < 2.5$  is “substantial” evidence in favor of a model,  $2.5 < \ln B < 5$  is “strong,” and  $\ln B > 5$  is “decisive.” Reprinted figure with permission from [Kitching et al. \(2008a\)](#), <http://link.aps.org/abstract/PRD/v77/e103008>.

This can be appreciated in the green and red narrow bands of [Figure 15.5](#).

Particle physics experiments that will be completed by the time of LSST do not guarantee a determination of the neutrino mass  $\Sigma m_\nu$  if it lies below 0.2 eV. Neutrino-less double beta decay experiments will be able to constrain neutrino masses only if the hierarchy is inverted and neutrinos are Majorana particles (i.e., their own anti-particle). On the other hand, oscillation experiments will determine the hierarchy only if the composition of electron flavor in all the neutrino mass states is large (i.e., if the mixing angle  $\theta_{13}$  is large). Cosmological observations are principally sensitive to the sum of neutrino masses. However, there is some sensitivity to individual masses, due to features in the power spectrum arising from the different redshifts when the neutrinos become non-relativistic. The effects are weak ([Slosar 2006](#)), but a large, deep weak lensing survey in combination with Planck, could exploit this signal and tighten the above constraints further. Thus, the LSST survey, together with CMB observations, could offer valuable constraints on neutrino properties highly complementary to particle physics parameters.

[De Bernardis et al. \(2009\)](#) parametrized neutrino masses using  $\alpha$ , where  $m_3 \equiv \alpha \sum m_\nu$  under the weak assumption that  $m_1 = m_2$ .  $\alpha \sim 1$  represents the normal hierarchy for very low mass of the lightest neutrino, and  $\alpha \simeq 0$  represents the inverted hierarchy. They compute the expected marginal error on  $\alpha$  for a fiducial model consistent with the direct hierarchy: this is shown in [Figure 15.6](#): distinguishing the hierarchy is within reach of a large-scale weak lensing survey such as could be undertaken with LSST, with an expected marginal error on  $\alpha$  of 0.22 (for normal hierarchy). [De Bernardis et al. \(2009\)](#) also point out that assumption of the wrong hierarchy can bias other cosmological estimates by as much as  $1 - 2\sigma$ .

These constraints have also been considered in the framework of Bayesian evidence ([Kitching et al.](#)

2008a). The Bayes factor is a tool for model selection, and can be used to quantify an experiment's ability to distinguish one model from another (§ B.3). The standard model predicts three neutrino species; corrections to account for quantum electrodynamics (QED) effects and for neutrinos being not completely decoupled during electron-positron annihilation imply  $N_{eff} = 3.04$ . Any light particle that does not couple to electrons, ions, and photons will act as an additional relativistic species. Departures from the standard model, which are described by a deviation  $N_{eff} \neq 3.04$ , can arise from the decay of dark matter particles, quintessence, exotic models, and additional hypothetical relativistic particles such as a light majoron or a sterile neutrino. Such hypothetical particles are constrained from standard big bang nucleosynthesis (BBN), where the allowed extra relativistic degrees of freedom are  $N_{eff}^{BBN} = 3.1_{-1.2}^{+1.4}$  (see e.g., Mangano et al. 2007). BBN constraints rely on different physics and the energy density in relativistic species may easily change from the time of BBN to the later Universe.

Figure 15.7 shows the predicted evidence for the number  $N_\nu$  of neutrinos from the analysis described above. The solid line shows the conditional evidence assuming that the other parameter is fixed at its fiducial value, the dashed line shows the marginal expected evidence when the possible values of the hidden parameter are taken into account. We see that only if  $N_{eff} > 3.4$  will the evidence against the standard model be decisive.

To summarize: the errors on the sum of the neutrino masses from a weak lensing analysis of a fiducial LSST survey are impressively small, and there is some sensitivity to individual neutrino masses, enough in principle to distinguish between the normal and inverted hierarchies. Improvement in constraints on the effective number of neutrinos is also possible, but the constraints are not expected to be particularly tight.

## 15.3 Testing Gravity

*Alan F. Heavens, Licia Verde*

### 15.3.1 Introduction

The acceleration of the Universe is such an unexpected feature that it has spawned a number of explanations, many of which are very far-reaching in their consequences. The simplest solution is found in Einstein's General Theory of Relativity (GR), in the form of the infamous cosmological constant. In a more modern guise, this term is placed on the opposite side of Einstein's field equation, as a source term, and is interpreted as a vacuum energy density. This opens up a wealth of more general possibilities that the source is not actually vacuum, but a slowly rolling dark energy field, which may evolve. Since this field would need to account for about 75% of the Universe's energy budget, determining its properties and nature is essential for a full understanding of the Universe. In addition to this possibility, there is an even more radical solution. As a cosmological constant, Einstein's term represents a modification of the gravity law itself, rather than an unusual source of gravity. Thus it is compelling to raise the question of whether the acceleration is driven by a new, beyond-Einstein theory of gravity. Although no compelling theory currently exists, suggestions include modifications to GR arising from extra dimensions, as might be expected from string theory braneworld models. There are potentially measurable effects of such exotic gravity

models that LSST could probe (e.g., [Lue et al. 2004](#); [Song 2005](#); [Ishak et al. 2006](#); [Knox et al. 2006a](#); [Zhang et al. 2007](#)), and finding evidence for extra dimensions would of course signal a radical departure from our conventional view of the Universe.

In this section we focus on measurements that might be made to distinguish GR from modified gravity models. We will restrict the discussion to scalar perturbations, and how they are related to observation. The interval in the conformal Newtonian gauge may be written in terms of two scalar perturbations,  $\psi$  being the potential fluctuation and  $\phi$  the curvature perturbation, as follows

$$ds^2 = a^2(\eta) [(1 + 2\psi)d\eta^2 - (1 - 2\phi)d\vec{x}^2], \quad (15.4)$$

where we assume a flat background Universe for simplicity. This assumption is easily relaxed.  $a(\eta)$  is the scale factor as a function of conformal time.

In GR, and in the absence of anisotropic stresses (a good approximation for epochs when photon and neutrino streaming are unimportant),  $\phi = \psi$ . In essence, the information is all contained in these potentials and how they evolve, and these will depend on the gravity model. In modified gravity, one expects that the Poisson law is modified, changing the laws for  $\psi$  and  $\phi$ . WL and spectroscopic galaxy surveys together can provide consistency tests for the metric perturbations, density fluctuations, and velocity field in the GR framework (e.g., [Zhang et al. 2007](#); [Song & Doré 2008](#)). Furthermore, ([Zhang et al. 2007](#)) show that the ratio of the Laplacian of the Newtonian potentials to the peculiar velocity divergence can be a clean probe of modified gravity – independent of galaxy-mass bias and the scale of mass perturbations.

The difference between  $\phi$  and  $\psi$  can be characterized ([Daniel et al. 2009](#)) by the *slip*,  $\varpi$ . Since this may be scale- and time-dependent, we define in Fourier space

$$\psi(k, a) = [1 + \varpi(k, a)] \phi(k, a), \quad (15.5)$$

where  $\varpi \equiv 0$  in GR. We may also write the modified Poisson equation in terms of the matter perturbation  $\delta_m$  and density  $\rho_m$  as ([Amendola et al. 2008](#))

$$-k^2\phi = 4\pi G a^2 \rho_m \delta_m Q(k, a), \quad (15.6)$$

which defines  $Q$  as an effective change in the Gravitational Constant  $G$ .

Different observables are sensitive to  $\psi$  and  $\phi$  in different ways ([Jain & Zhang 2008](#)). For example, the ISW effect depends on  $\dot{\psi} + \dot{\phi}$ , but the effect is confined to large scales, and cosmic variance precludes accurate use for testing modified gravity. Peculiar velocities are sourced by  $\psi$ , and LSST may be a useful source catalog for later spectroscopic surveys to probe this. Lensing is sensitive to  $\psi + \phi$ , and this is the most promising route for LSST to probe beyond-Einstein gravity. The Poisson-like equation for  $\psi + \phi$  is

$$-k^2(\psi + \phi) = 2\Sigma \frac{3H_0^2 \Omega_m}{2a} \delta_m, \quad (15.7)$$

where  $\Sigma \equiv Q(1 + \varpi/2)$ . For GR,  $Q = 1$ ,  $\Sigma = 1$ , and  $\varpi = 0$ . The Dvali-Gabadadze-Porrati (DGP) braneworld model ([Dvali et al. 2000](#)) has  $\Sigma = 1$ , so mass perturbations deflect light in the same way as GR, but the growth rate of the fluctuations differs. Thus we have a number of possible

observational tests of these models, including probing the expansion history, the growth rate of fluctuations, and the mass density-light bending relation.

Some methods, such as study of the luminosity distance of Type Ia supernovae (SNe; e.g., [Riess et al. 1998](#)), baryonic acoustic oscillations (BAO; e.g., [Eisenstein & Hu 1998](#)), or geometric weak lensing methods (e.g., [Taylor et al. 2007](#)) probe only the expansion history, whereas others such as three-dimensional cosmic shear weak lensing or cluster counts can probe both. Models with modified gravity laws predict Universe expansion histories which can also be explained with standard GR and dark energy with a suitable equation of state parameter  $w(z)$ . In general, however, the growth history of cosmological structures will be different in the two cases, allowing the degeneracy to be broken (e.g., [Knox et al. 2006a](#); [Huterer & Linder 2007](#); but see [Kunz & Sapone 2007](#)).

### 15.3.2 Growth Rate

The growth rate of perturbations in the matter density  $\rho_m$ ,  $\delta_m \equiv \delta\rho_m/\rho_m$ , is parametrized as a function of scale factor  $a(t)$  by

$$\frac{\delta_m}{a} \equiv g(a) = \exp \left\{ \int_0^a \frac{da'}{a'} [\Omega_m(a')^\gamma - 1] \right\}, \quad (15.8)$$

where  $\Omega_m(a)$  is the density parameter of the matter. In the standard GR cosmological model,  $\gamma \simeq 0.55$ , whereas in modified gravity theories it deviates from this value ([Linder 2005a](#)). As a strawman example, the flat DGP braneworld model ([Dvali et al. 2000](#)) has  $\gamma \simeq 0.68$  on scales much smaller than those where cosmological acceleration is apparent ([Linder & Cahn 2007](#)). While this is not the most general model (in principle  $\gamma$  might, for example, depend on scale) this offers a convenient Minimal Modified Gravity parametrization ([Linder & Cahn 2007](#); [Huterer & Linder 2007](#)).

Measurements of the growth factor can be used to determine the growth index  $\gamma$ . It becomes a very interesting question to ask whether a given method or observational set up could distinguish between the dark energy and modified gravity scenarios. In contrast to *parameter estimation*, this is an issue of *model selection*, which has been the subject of recent attention in cosmology. That is, one might compare a dark energy model that has a fixed GR value for  $\gamma$  with a modified gravity model whose  $\gamma$  is determined by the data and ask “do the data require the additional parameter and therefore signal the presence of new physics?” This question may be answered with the Bayesian evidence,  $B$ , which is proportional to the ratio of probabilities of two or more models, given some data (see § B.3 for more details). To quantify how LSST will help in addressing the issue of testing gravity using the growth of structures, we follow [Heavens et al. \(2007\)](#).

[Figure 15.8](#) shows how the Bayesian evidence for GR changes with increasing true deviation of  $\gamma$  from its GR value for a combination of a Stage 4 WL survey (comparable to our fiducial LSST survey) and Planck ([Heavens et al. 2007](#)). The expected evidence ratio changes with progressively greater differences from the GR growth rate. The combination of WL and Planck could strongly distinguish between GR and minimally-modified gravity models whose growth index deviates from the GR value by as little as  $\delta\gamma = 0.048$ . Even with the WL data alone, one should be able to decisively distinguish GR from the DGP model at  $\ln B \simeq 11.8$ , or, in the frequentist view,  $5.4\sigma$  ([Heavens et al. 2007](#)). The combination of WL+Planck+BAO+SN should be able to distinguish

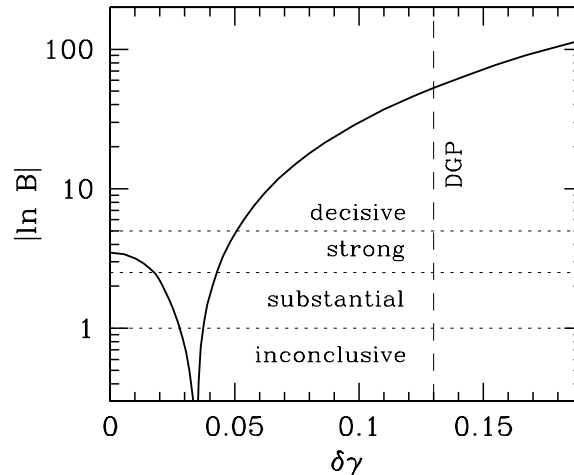


Figure 15.8: Bayesian evidence  $B$  for GR as a function of the true deviation of the growth index from GR,  $\delta\gamma = \gamma - 0.55$ , for a Stage 4 WL survey comparable to our fiducial survey in combination with Planck. The larger the  $B$  value, the greater the statistical power of this survey to distinguish the models. If modified gravity is the true model, GR will be favored by the data to the left of the cusp ( $B > 1$ ), and increasingly disfavored to the right ( $B < 1$ ). The Jeffreys scale of evidence (Jeffreys 1961) is as labeled. Joint BAO and WL will place stronger constraints. Figure from Heavens et al. (2007), with permission.

$\delta\gamma = 0.041$  at  $3.41\sigma$ . A vacuum energy General Relativity model will be distinguishable from a DGP modified-gravity model with log evidence ratio  $\ln B \simeq 50$  with LSST + Planck; the three-dimensional lensing data alone should still yield a “decisive”  $\ln B \simeq 11.8$ . An alternative approach is to explore whether the expansion history and growth rate are consistent assuming GR (Lue et al. 2004; Song 2005; Ishak et al. 2006; Knox et al. 2006a).

Next we turn to constraints on the slip. Considering a simplified model (Daniel et al. 2009), where  $\varpi = \varpi_0(1+z)^{-3}$  is a specific function of scale factor only, the expected errors on  $\varpi_0$ , after marginalizing over other cosmological parameters, are shown in Figure 15.9. We see that LSST could improve vastly on what is currently possible.

An alternative approach is to look for inconsistencies in the  $w$  derived from the growth rate and that derived from the distance-redshift relation. Given a dark energy parameter, such as the energy density  $\Omega_\Lambda$  or equation of state  $w$ , we split it into two parameters with one controlling geometrical distances, and the other controlling the growth of structure. Observational data are then fitted without requiring the two parameters to be equal. Recently, Wang et al. (2007) applied this *parameter-splitting* technique (Simpson & Bridle 2005; Zhang et al. 2005; Zhan et al. 2009) to the current data sets, and Figure 15.10 shows the main result. It reveals no evidence of a discrepancy between the two split meta-parameters. The difference is consistent with zero at the  $2\sigma$  level for the quintessence(Q)-CDM model. The existing data sets already pose tight constraints on  $w$  derived from geometry. However, the constraint is much weaker for  $w$  derived from growth, because currently galaxy data are limited by the uncertainty of the bias factor and WL data are restricted by both the width and depth of the survey. LSST will open these windows dramatically.

The parameter-splitting technique can also check for *internal* inconsistency within any *one* data set, such as shear tomography, that is sensitive to both geometry and growth. It can be thought of as a crude way to parametrize the space of these theories. As such, the constraints can be viewed

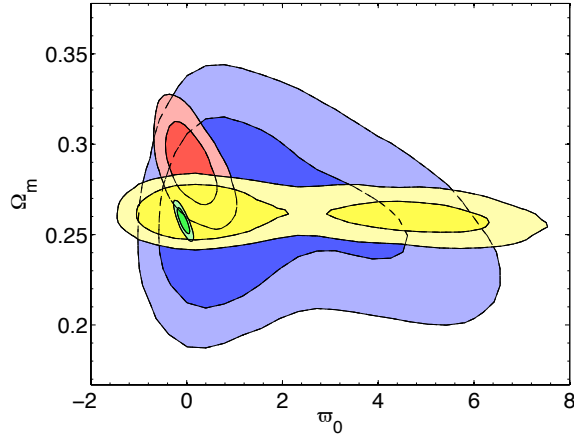


Figure 15.9: Projected 68% and 95% likelihood contours of the matter fraction  $\Omega_m$  and gravitational slip  $w_0$  for WMAP 5-year data (blue), adding current weak lensing and ISW data (red). Yellow is mock Planck CMB data, and green adds weak lensing from a 20,000  $\text{deg}^2$  survey. Figure from Daniel et al. (2009), with permission.

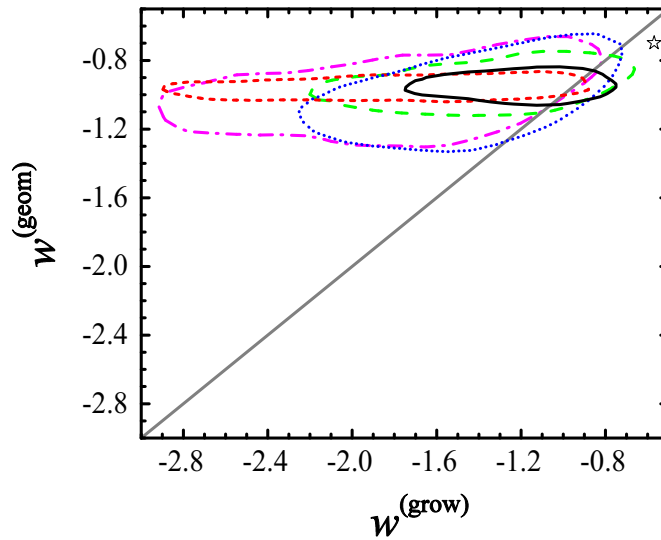


Figure 15.10: Joint constraints on  $w(\text{geom})$  and  $w(\text{grow})$  in a model in which the two EOS parameters are allowed to be different. The contours show the 68% confidence limits from the marginalized distributions. The thick gray line shows  $w(\text{geom}) = w(\text{grow})$ . Different contours and curves represent constraints from different combinations of the current data sets (CMB, SNe, galaxies and WL). The smallest contour and the most narrow curve (black solid line) represent constraints from all the data. No significant difference is found and deviations are constrained to  $w(\text{geom}) - w(\text{grow}) = 0.37^{+0.37+1.09}_{-0.36-0.53}$  (68% and 95% C.L.). The star-shaped symbol corresponds to the effective  $w(\text{geom})$  and  $w(\text{grow})$ , which approximately match the expansion history and the growth history, respectively, of a flat DGP model with our best-fit  $\Omega_m$ . Adapted from Wang et al. (2007).

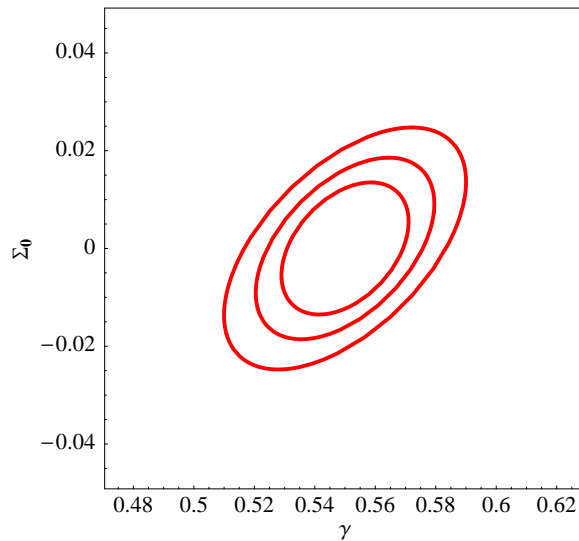


Figure 15.11: Projected 68% likelihood contours of  $\Sigma$ , the parameter describing the effective modification to the lensing potential, and the growth index  $\gamma$  for weak lensing surveys from a full sky survey with median  $z = 0.9$ , and surface densities of sources of 35, 50, and 75 galaxies per arcminute. LSST is likely to achieve a surface density near the bottom of this range. Errors scale inversely with the square root of the sky fraction. Figure from [Amendola et al. \(2008\)](#), with permission.

as putting restrictions on modified gravity theories, with the caveat that the precise constraints on any particular theory must be worked out on a case by case basis.

Finally, we show in [Figure 15.11](#) how accurately LSST could measure evolution of  $\Sigma$ , which describes the modification to the lensing potential ([Equation 15.7](#)). Assuming  $\Sigma = 1 + \Sigma_0 a$ ,  $\Sigma_0$  may be determined to an accuracy of a few hundredths ([Amendola et al. 2008](#)). One caveat on all of these conclusions is that WL requires knowledge of the nonlinear regime of galaxy clustering, and this is reasonably well-understood for GR, but for other models, further theoretical work is required. This has already started ([Schmidt et al. 2008](#)).

## 15.4 Anisotropic Dark Energy and Other Large-scale Measurements

*Anthony Tyson, Hu Zhan*

By providing measurements of WL shear, BAO, and other observables in different directions on the sky covering  $\sim 100^\circ$  scales, LSST will address specific questions related to clustering on the largest scales. These range from the clustering of dark energy to exotic models that require horizon scale tests (see also [§ 13.4](#) and [§ 13.7](#)). Because of its wide and deep coverage, the 20,000  $\text{deg}^2$  LSST survey of billions of galaxies has the power to test isotropy to percent level precision.

There is compelling evidence that the mean expansion of the Universe is accelerating. At this time there are no plausible theoretical models for the dark energy. We are far from understanding

the nature of this phenomenon. In some respects this is similar to the earliest days of the CMB observations. We should, therefore, examine the consequences of an anisotropic dark energy in cosmological models and estimate their observability.

While there are even fewer plausible theories of anisotropic dark energy, there are several logical possibilities that can be checked through direct observation. It is in principle possible to have anisotropy in an otherwise homogeneous Universe described by a cosmological constant. If dark energy is something other than a cosmological constant, it will in general have anisotropic stresses at some level. This is also a generic prediction of modified gravity theories. Because covariance implies that a time-varying field is equivalently spatially-varying, dynamical dark energy is necessarily inhomogeneous. Inhomogeneities in the surrounding radiation and matter fields can drive fluctuations in dynamical dark energy. Spatial variations in the expansion rate should accompany fluctuations in dark energy. Distortions of the expansion rate and luminosity distance may also arise if the observed cosmic acceleration is due to gravitational effects in a strongly inhomogeneous Universe.

In some models the small Jeans scale of the effective dark energy forms small wavelength perturbations which can be probed via weak lensing (Amendola et al. 2008). In general, it may be possible to distinguish between cosmological constant, dynamical dark energy, and modified gravity. Jiménez & Maroto (2007) studied the consequences of a homogeneous dark energy fluid having a non-vanishing velocity with respect to the matter and radiation large-scale rest frames. They found that in scaling models, the contributions to the quadrupole can be non-negligible for a wide range of initial conditions. Anisotropies have been considered as potentially observable consequences of vector theories of dark energy (Armendáriz-Picón 2004).

#### 15.4.1 Possible Relation to CMB Large Scale Anisotropy

The CMB exhibits less power on large scales than predicted (Spergel et al. 2003). Perhaps this is a statistical fluke, due to cosmic variance in an ensemble of possible universes. However, we should also explore alternative explanations. Perturbations whose wavelengths enter the horizon concurrent with dark energy domination distort the CMB during the late time acceleration. Is the cosmological principle more fundamental than general relativity? It is worthwhile to observationally study this assumption of perfect homogeneity on large scales. We know that large inhomogeneities exist on smaller scales. Large scale CMB anisotropies develop for off-center observers in a spherically symmetric inhomogeneous universe (Alnes & Amarzguioui 2006; Enqvist & Mattsson 2007). Koivisto & Mota (2008) investigated cosmologies where the accelerated expansion of the Universe is driven by a field with an anisotropic pressure. In the case of an anisotropic cosmological constant, they find that in the current data the tightest bounds are set by the CMB quadrupole.

#### 15.4.2 Matter Inhomogeneities

One might ask if we can tell the difference between anisotropic matter cosmic variance and dark energy cosmic variance. Depending on the redshift, that could be settled by looking at the galaxy number count quadrupole, etc. over a cosmological volume. What effects might be present in

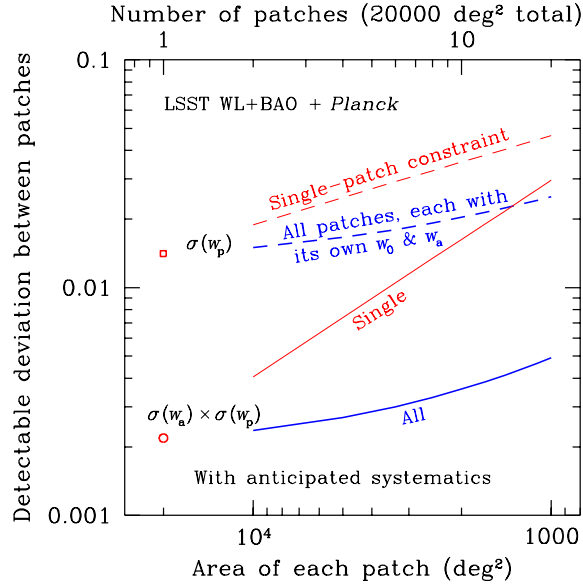


Figure 15.12: Detectable deviation between LSST measurements of dark energy parameter,  $w_p$ , and error product as a function of the number of patches. The constraints are derived from the joint BAO and WL (galaxy–galaxy, galaxy–shear, and shear–shear power spectra) analysis in § 15.1. Note that there is little degradation in sensitivity as one goes from quadrupole to higher moments if the other marginalized cosmological parameters are shared: a 16 patch survey degrades the error product per patch by less than a factor of two. The red curves labeled “single” are for independent determination of all parameters for each patch. Estimated LSST systematics are included.

LSST data if there were an anisotropic distribution of matter on Gpc scales (viz. Caldwell & Stebbins 2008)? Our current framework for cosmology will be violated if the anisotropy is at a level well above the cosmic variance. If the cosmological principle does not hold, we cannot assume that physics here applies to other places in the Universe. Hence, there is a logical inconsistency in predicting observables for a truly anisotropic Universe (i.e., more anisotropic than allowed by cosmic variance) based on the Friedman-Robertson-Walker (FRW) model. Anisotropic matter is in some sense worse than anisotropic dark energy, only because we know more about matter fluctuations and hence their cosmic variance. Our ignorance about the appropriate cosmic variance for dark energy gives us some room for anisotropy.

### 15.4.3 Observations Enabled by LSST

Anisotropic dark energy can be probed via distance and growth measurements over the sky with all the dark energy probes. LSST is particularly suited for testing the anisotropy of dark energy. Its wide survey area enables one to measure dark energy properties in many patches and to potentially detect their variations across the sky; its deep imaging not only results in more usable galaxies for more accurate measurements of the distances and growth function, but also allows one to probe the differences in the evolution of dark energy properties across the patches.

The results of dark energy anisotropy tests using the joint LSST BAO (galaxy power spectra) and WL (shear power spectra) analysis are shown in Figure 15.12. See § 15.1 for details of the calculation such as the anticipated systematics and priors. The only difference from § 15.1 is that

we let each patch of sky have its own  $w_0$  and  $w_a$  in this section. The rest of the parameters are assumed not to vary from patch to patch and, thus, are shared among the patches.

In [Figure 15.12](#) we find only a small degradation in sensitivity to the dark energy EOS parameters that are allowed to vary independently in up to  $\sim 10$  different patches of the LSST survey area, if the other marginalized cosmological parameters are shared between patches. Each patch achieves nearly the same precision of measurement of the dark energy parameters as the full 20,000 deg<sup>2</sup> survey. For comparison, the red curves labeled “single” are for independent determination of all parameters for each patch. The single patch  $\sigma(w_p)$  line (and the single patch error product) is what one would get from just doing the LSST survey over that smaller patch area.

In the single patch case, the Fisher matrix (see [§ B.4.2](#)) is proportional to the area of the survey<sup>3</sup>, so that the estimated error on a single parameter scales as square root of the number of patches,  $N_{\text{pat}}$ , and the error product  $w_p \times w_a \propto N_{\text{pat}}$ . Because  $w_0$  and  $w_p$  consist only a small subset of many cosmological and nuisance parameters that BAO and WL can constrain, increasing the degrees of freedom of the dark energy EOS to  $2N_{\text{pat}}$  does not inflate individual parameter errors by a factor of  $N_{\text{pat}}^{1/2}$ . Therefore, the “all” results in [Figure 15.12](#) degrades more slowly than the “single” results.

Adding SNeIa would have little impact in [Figure 15.12](#), just as they do over the whole sky (see [Figure 15.3](#)). A SN-only survey will behave very much like the single patches in [Figure 15.12](#), because the only shared parameter among all patches on which SNeIa have some marginal constraint is curvature; in particular, the evolution parameters are not constrained. In other words, the gain of the “all” results over the “single” results is due to sharing these parameters across the sky.

A separate investigation using the angular power spectrum of SNeIa luminosity by [Cooray et al. \(2008\)](#) finds that an LSST-like survey of one million SNeIa at  $z \lesssim 1$  can limit rms dark energy fluctuations at the horizon scale down to a fractional energy density of  $\sim 10^{-4}$ . This limit is much higher than the  $1.92 \times 10^{-5}$  horizon-scale matter fluctuations measured from COBE ([Bunn & White 1997](#)), but as we have demonstrated above with the dark energy EOS, one can combine more LSST probes as well as external data sets to improve the constraints on dark energy density fluctuations.

## 15.5 Cosmological Simulations

*Salman Habib, Risa H. Wechsler*

An enormous amount of science can be extracted from a synoptic survey as deep, wide, and rich as LSST. In order to maximize the quantity and quality of the science, the underlying theory must be developed – as far as possible – to a point where analysis and interpretation of the data are not systematics-limited. In contrast to the analysis of the CMB temperature anisotropy, where, for the most part, only linear physics need be considered, predictions for LSST observations and analysis of the data will overwhelmingly involve nonlinear aspects of structure and galaxy formation. The nonlinear aspects include gravity, hydrodynamics, and a variety of astrophysical feedback mechanisms. Cosmological numerical simulations thus play a critical role in combining

<sup>3</sup>CMB observations are reduced to the same area.

these into a precision theoretical framework. Meeting the demands of LSST requires a numerical simulation campaign at the cutting edge of present and future computational astrophysics and cosmology.

### 15.5.1 The Simulation Context

In the context of a deep, wide survey such as LSST, which is exploring new regimes in parameter space, there are four general uses for cosmological simulations. The first is an accurate calculation of the underlying dark matter framework for a given cosmological model. Because dark matter outweighs baryons by roughly a factor of five, gravity-only N-body simulations provide the bedrock on which all other techniques rest. The second use is a detailed prediction of the observed galaxy population and other observables in the survey, including all relevant baryonic effects. Third, simulation based mock-catalogs provide an essential tool for the planning of the LSST survey strategy and for testing its technical aspects. The final critical use of simulations is to provide a framework for interpreting the LSST data in the context of models, both cosmological models and models of baryonic physics.

These different uses require a wide range of input physics into the simulation. Ideally, we would like to be able to simulate the full structure formation problem, including galaxy and star formation, in a box the size of the LSST survey volume. However, it will not be possible now, or in the foreseeable future, to develop an accurate first principles simulation capability that can address the needs of all of the observational probes enabled by LSST; the dynamic range is too vast and the underlying physics too complex. On the largest scales where gravity from dark matter dominates, gravity-only simulations are sufficient for predictions of structure. However, on scales smaller than a few Mpc, complex baryonic physics also enters requiring the modeling of (magneto-)hydrodynamic, thermal, chemical, and radiative processes. The computational challenges are immense, even in the dark matter only case, and become prohibitive when solving the full baryonic problem.

To overcome the computational hurdle, several strategies exist. To begin with, we will need to produce a large, LSST-volume simulation of the dark matter distribution at modest resolution with as many simulation particles as possible. This will provide the backbone of the simulation analysis. What is required is a collection of robust phenomenological approaches for combining the observations with simulation results, appropriately tuned for each of the observational probes. We will refer to these approaches collectively as examples of “self-calibration.” One technique is to incorporate results from hydrodynamic simulations done over small yet representative volumes by developing semi-analytic models that can be used in large-volume, gravity-only simulations. Statistical methods can also be used to add galaxies to the N-body simulation. These should reproduce the observed distribution of galaxies with as much fidelity as possible based on existing data, including upcoming stage III experiments such as DES and PanSTARRS as well as the results from deeper smaller volume surveys from the ground and from space.

A more computationally intensive approach is the use of large-scale hydrodynamical simulations with sub-grid models developed using smaller runs. As simulation capabilities continue their explosive growth (supercomputer performance has increased by a factor of 10,000 over the last 15 years), we can expect a major improvement in the sophistication of self-calibration techniques over what is available now. Indeed, many of the phenomenological modeling ideas currently in use will

be obsolete by the time the LSST data stream is in full flow. The LSST simulation campaign must have the flexibility to change as this situation evolves.

Finally, LSST is developing a detailed image simulation pipeline, described in § 3.3, which uses the properties of galaxies in cosmological simulations as a key input. These simulations are essential for developing the data reduction, management, and analysis pipelines and also provide critical input to the various science teams in planning and running their analysis.

It is also important to keep in mind that, because LSST will exist on the same timescale as other important large scale structure probes (JDEM, eROSITA, SKA), there will be substantial overlap in the simulation requirements. The power of combining various data sets will significantly lower the systematics floor and impose additional demands on simulations. For example, the simple dark energy parametrizations currently in use may have to be abandoned in favor of a non-parametric approach embedded within the simulation framework. Additionally, an advanced framework of simulations will be necessary in guiding how we combine the multiple data sets from different surveys. This will become easier as computer power grows enabling “end-to-end” style modeling.

### 15.5.2 LSST Simulations I: Main Requirements

The large-scale distribution of matter (on scales greater than several Mpc) is determined primarily by gravity. Therefore, the first set of simulation desiderata are determined by what is required of N-body simulations. For LSST, the largest scales of interest cover studies of Baryon Acoustic Oscillations (BAO), which occur on scales of  $150 h^{-1}\text{Mpc}$ . LSST BAO studies will require 0.1% accuracy for the matter power spectrum to scales  $k \sim 0.3 h\text{Mpc}^{-1}$  over a range of redshifts  $0.1 < z < 5$  (for a recent discussion of BAO simulation errors, see [Nishimichi et al. 2008](#)). In the high redshift range, perturbation theory may suffice, but for  $z < 1$ , perturbative results rapidly lose accuracy in ways that are difficult to predict ([Carlson et al. 2009](#)). In any case, the mock catalogs required to develop BAO analysis as well as to understand the dependence on galaxy properties can only be carried out with simulations.

Additionally, the cluster-scale halo mass distribution and its dependence on cosmology can be calibrated with N-body simulations. It is already known to be non-universal in a way that can influence precision cosmological analyses ([Reed et al. 2007](#); [Lukić et al. 2007](#); [Tinker et al. 2008](#); [Lukić et al. 2009](#); [Bhattacharya et al. 2009](#)). Because significant constraints come from the high end of the mass function, where the number density drops exponentially, simulation of large volumes are also needed to more accurately characterize the mass function in this range.

In general, the N-body simulation task for galaxy clustering and cluster counts is targeted at precision studies of the dark matter halo and subhalo distribution, construction of sufficiently fine-grained merger trees for improved empirical and semi-analytic modeling of the galaxy distribution, and running a large number of simulations to understand errors and their covariances. The fundamental science requirements are: 1) sufficient mass resolution to resolve dark matter halos and subhalos hosting the target galaxies, 2) sufficient volume to control sample variance uncertainties, and 3) enough information to model galaxy bias. For LSST, this translates into simulations with multi-Gpc box-sizes and particle counts in the  $10^{11-12}$  range (for mass resolutions of order  $10^9 M_\odot$ ), all with  $\sim\text{kpc}$  force resolution. These simulations will probe the scales of superclusters, voids, and

large-scale velocity fields, and are well-matched to petascale computing resources (Habib et al. 2009).

Full-up simulations of this kind cannot be performed with petascale resources but require going to the exascale: resolving subhalos in a Hubble volume demands  $10^{13-14}$  particles, in turn requiring  $10^{24}$  flop of computation. By 2015, assuming current trends hold, computing performance will be at the 100 Petaflop level. Therefore, provided that N-body code development keeps pace with architecture developments, simulations at the scale demanded by LSST will be available by the time the data makes its appearance.

While such simulations will provide a significant amount of power for understanding the LSST data, they need additional refinement. In particular, we will need targeted simulations which investigate higher resolution to calibrate the impact of the smaller scale clustering and simulations including gas physics to understand the impact of baryons on the dark matter distribution. Finally, we will need models for putting LSST observables into the N-body simulations. These models can take the form of direct hydrodynamical simulations of small scales, semi-analytic modeling of high-resolution merger trees that incorporate sub-grid physics calibrated to the higher resolution simulations, and empirically constrained statistical models for incorporating the observational galaxy distribution into the simulation.

Simulations with smaller box sizes (linear scales of Gpc and less) are needed to deal with further challenges posed by LSST weak lensing observations, requiring absolute error control at the sub-percent/percent level up to scales of  $k \sim 10 \text{ hMpc}^{-1}$  (Huterer & Takada 2005). Currently, the best demonstrated N-body error control is at the 1% level out to  $k \sim 1 \text{ hMpc}^{-1}$  (Heitmann et al. 2008), and this can be extended and improved to  $k \sim 10 \text{ hMpc}^{-1}$  with a petascale computing campaign.

Recent studies have shown that the evolution of the baryonic component of the Universe imprints itself even on the largest scales, including a roughly 5% impact on the cluster mass function and the BAO peak (Stanek et al. 2009). This is also true on larger scales than may have been expected for the weak lensing power spectrum; baryonic effects become important beyond scales of  $k \sim 1 \text{ hMpc}^{-1}$  (White 2004; Zhan & Knox 2004; Jing et al. 2006; Rudd et al. 2008). This creates a systematic error present in any attempt to extract cosmological parameters calibrated using N-body only simulations. Unfortunately, the computational power necessary for even a rough treatment of the baryons on the LSST scales is not present. It will, therefore, be necessary to complement our above large volume simulations with a series of much smaller, higher-resolution simulations that include accurate treatment of the gas physics. Although a full treatment will require AMR and SPH simulations with absolute error controls and physics treatments beyond the current state of the art, there are encouraging signs that self-calibration approaches can be used successfully. In particular, Zentner et al. (2008, see also § 14.5.4) showed that the impact of baryonic physics on the weak lensing power spectrum can be measured from hydrodynamic simulations and added as a correction to dark matter only simulations with high accuracy.

Similar self-calibration approaches can be applied to modeling cluster counts, which for LSST will be in the hundreds of thousands. The critical requirement for simulations is to properly model the form of various mass–observable relations; the parameters specifying this form can then be self-calibrated with the data itself (e.g., Rozo et al. 2009). Still, it is essential to determine the sensitivity of these relations to baryonic treatment and the full range cosmological parameter space.

Although this is a very large computational task, petascale capabilities are sufficient to accomplish it within the next few years.

The associated simulations are an order of magnitude more expensive than the underlying pure N-body runs, and extensive numerical exploration is required to understand the effects of parametric variations in sub-grid models. Additionally, it must be kept in mind that modeling of various sources of systematic error, such as intrinsic galaxy alignments (§ 14.5.3) and the photometric redshift distribution, is actually a bigger concern for weak lensing measurements, and will require substantial observational input.

Finally, resolving the smallest length scales using a series of nested boxes will be necessary for investigating the physics and dark matter and baryonic structure of individual galaxies and galaxy clusters. These simulations will be useful for providing an additional source of sub-grid inputs into the large-scale codes and will also be essential for weak and strong lensing studies of cluster masses especially the influence of substructure. Detailed simulations for investigations of the properties of dark matter-dominated dwarf satellite galaxies of the Milky Way are needed, incorporating modifications of CDM (e.g., warm and interacting dark matter). Detecting these galaxies is a prime target for LSST as described in Chapters 7 and 9.

Given the computational challenges of hydrodynamical simulations, as well as the fact that they still involve significant unresolved sub-grid physics that impacts the observations, it is essential to develop in parallel empirical and semi-analytic models for connecting the well-modeled dark matter distribution with the observed galaxy distribution. Current approaches range from those which require resolved substructure (Conroy et al. 2006), to halo occupation approaches (Berlind & Weinberg 2002) that only require resolving central halos, to algorithms which are designed specifically for modeling larger volumes with poor resolution (ADDGALS; Wechsler et al. 2009). Generically, these models use available data to constrain a statistical relation between the observed galaxy and properties of the dark matter distributions. Such models let us build mock galaxy catalogs that are designed to reproduce particular observed galaxy properties, such as clustering, bias, and mass-richness relations. These models can be run on top of the lightcone outputs of N-body simulations to create mock catalogs that will help us bridge this gap between dark matter simulations and observable properties. Indeed, with the level of precision that modern cosmology has reached, understanding of the dark matter-observable relation will likely be a dominant source of error when extracting cosmological information from LSST data.

The requirements of such mock catalogs for LSST are quite stringent. In order to test the full analysis pipeline, these catalogs should produce galaxies with realistic photometric and morphological properties down to  $r = 28$  and cover as much volume as possible, and must be produced for a range of cosmological models (described more fully in the following section). Additionally, mocks should include the correlation between galaxy properties and, for example, AGN properties and supernovae, and should include the full range of source light curves is needed to model the types of variability that will be seen by LSST.

### 15.5.3 LSST Simulations II: New Directions

Aside from investigating the role of dark energy as a background phenomenon, LSST observations can put constraints on dark energy anisotropy and clustering, enable tests of gravity on cosmological

and astrophysical scales, investigate the primordial density fluctuation power spectrum including the existence of features and running of the spectral index, and study primordial non-Gaussianities (§ 13.4.2). A suite of simulations must be developed to address all of these questions. Most of the simulation capability would be based around that discussed above, but several new directions will be explored.

Fully self-consistent simulations for dynamical dark energy models, with initial conditions set by transfer functions incorporating dark energy fluctuations, will be necessary to make realistic predictions for LSST observations. Because dark energy clustering occurs on very large scales, the basic simulation requirements are not too different from those for galaxy clustering. The added wrinkle will be the need for a PDE-solver for the quintessence field, but the dynamic range for this is limited and will not be a significant overhead.

Investigations of the primordial power spectrum essentially involve running the standard simulations but with a modified initial condition. Although large scales may be in the linear or quasi-linear regime, simulations are important in understanding systematics issues, such as the role of scale-dependent bias and modeling of galaxy evolution. Explorations outside the simple assumptions underlying current approaches (adiabatic Gaussian fluctuations, power-law primordial spectra) are essential to establish the robustness of inferences made from the observations, especially since – the inflationary paradigm notwithstanding – there is no firmly established theory of initial conditions. An example of this sort of exploration is scale-dependent halo bias induced by non-Gaussianity (Dalal et al. 2008; Matarrese & Verde 2008, see also § 13.4.2) in the initial conditions. Primordial non-Gaussianity has been traditionally parametrized by the parameter,  $f_{NL}$ , which LSST can constrain extremely tightly (to  $f_{NL} \sim 1$ , Carbone et al. 2008), however, this is only a particular case, and other aspects of non-Gaussianity should be investigated (for example, by using the Edgeworth expansion to set up initial conditions).

Simulations aiming to study the effects of modified gravity are based either on the use of specific models or on the so-called parametrized post-Friedmann approach, which uses one post-Newtonian parameter,  $\gamma$ , to signify departures from general relativity (e.g., Bertschinger & Zukin 2008). Simulations such as Stabenau & Jain (2006), Laszlo & Bean (2008), Oyaizu (2008), and others that include long-range dark matter interactions (Nusser et al. 2005), will be useful foils for the main line of the numerical effort, important to clarify the precise nature of LSST observational results (in terms of acceptance or rejection of alternative models).

### 15.5.4 Calibration Frameworks

The simulation requirements for next-generation cosmological surveys such as LSST are very demanding and cover not only scanning over cosmological and physical modeling parameters, but in the case of end-to-end modeling, a slew of observational and instrumental variables. The final number of parameters can range from tens to thousands, depending on the particular application. While post-processing results from expensive simulations can sometimes be used to incorporate more parameters, this approach is far from being universal. The basic difficulty that must be faced is that the number of complex simulations that can be performed will always be finite – based on this finite set of results, one has to effectively interpolate across a high-dimensional space of parameters.

The most direct way to approach this problem is through a brute-force comparison of simulated output with the most recent observational data. A number of upcoming surveys are expected to be in the final stages of taking data by the time LSST comes online in 2015. In particular, the Dark Energy Survey (DES) and Pan-STARRS are expected to map out thousands of square degrees down to 24th magnitude, roughly the depth of a single LSST exposure.

Incorporating observational information such as color distributions and clustering from these surveys into, for example, galaxy halo occupation distribution (HOD) modeling, as well as comparing with predictions from hydro simulations and semi-analytic modeling, will be necessary to begin immediate analysis of the LSST data as it becomes available. In particular, this will allow us to create a stronger understanding of our mass-observable relations, and, with the help of a realistic transfer function for creating mock sky images, can help in getting an initial handle on systematics. However, these comparisons will only help to understand how to accurately represent the galaxy distribution of a given (simulated) cosmology and set of model parameters, making it very difficult to scan across a wide range of cosmological models, not all of which will have been directly simulated.

Recent advances in applications of Bayesian and other statistical techniques to modeling simulation results has resulted in the development of the cosmic calibration framework (Heitmann et al. 2006; Habib et al. 2007; Schneider et al. 2008), an approach targeted precisely to the problem identified above. Given a smooth enough response surface in the high-dimensional parameter space, this methodology has been shown to give excellent results, in particular, percent level predictions for the nonlinear matter power spectrum (Heitmann et al. 2009). The procedure consists of four interlocking steps: 1) defining the simulation design, which determines at what parameter settings to generate the training sets, 2) generation of the emulator – using PCA-based Gaussian process models – which replaces the simulator as a predictor of results away from the points that were used to generate the training set, 3) an uncertainty and sensitivity analysis associated with the emulator, and 4) the (self-) calibration against data via MCMC methods to determine parameter constraints. The calibration methodology can be adapted to multiple tasks within the LSST science campaign and, significantly, can be used similarly for cosmological parameters, the parameters specifying the empirical or semi-analytic models, as well as uncertainties in the instrumental response. In each case unknown parameters can be determined in the final MCMC calibration against observational results.

## References

- Albrecht, A. et al., 2009, ArXiv e-prints, 0901.0721  
Albrecht, A., & Bernstein, G., 2007, *Phys. Rev. D*, 75, 103003  
Albrecht, A. et al., 2006, ArXiv Astrophysics e-prints, astro-ph/0609591  
Alnes, H., & Amarzguioui, M., 2006, *Phys. Rev. D*, 74, 103520  
Amendola, L., Kunz, M., & Sapone, D., 2008, *Journal of Cosmology and Astro-Particle Physics*, 4, 13  
Armendáriz-Picón, C., 2004, *Journal of Cosmology and Astro-Particle Physics*, 7, 7  
Barnard, M., Abrahamse, A., Albrecht, A., Bozek, B., & Yashar, M., 2008, *Phys. Rev. D*, 78, 043528  
Berlind, A. A., & Weinberg, D. H., 2002, *ApJ*, 575, 587  
Bernstein, G., 2006, *ApJ*, 637, 598  
Bertschinger, E., & Zukin, P., 2008, *Phys. Rev. D*, 78, 024015  
Bhattacharya, D. et al., 2009, in prep.

- Bunn, E. F., & White, M., 1997, *ApJ*, 480, 6
- Caldwell, R. R., & Stebbins, A., 2008, *Phys. Rev. Lett.*, 100, 191302
- Carbone, C., Verde, L., & Matarrese, S., 2008, *ApJL*, 684, L1
- Carlson, J., White, M., & Padmanabhan, N., 2009, Astrophysics eprint, 0905.0479
- Castro, P. G., Heavens, A. F., & Kitching, T. D., 2005, *Phys. Rev. D*, 72, 023516
- Conroy, C., Wechsler, R. H., & Kravtsov, A. V., 2006, *ApJ*, 647, 201
- Cooray, A., Holz, D. E., & Caldwell, R., 2008, ArXiv e-prints, 0812.0376
- Dalal, N., Doré, O., Huterer, D., & Shirokov, A., 2008, *Phys. Rev. D*, 77, 123514
- Daniel, S. F., Caldwell, R. R., Cooray, A., Serra, P., & Melchiorri, A., 2009, ArXiv e-prints, 0901.0919
- De Bernardis, F., Kitching, T. D., Heavens, A., & Melchiorri, A., 2009, ArXiv e-prints, 0907.1917
- Dunkley, J. et al., 2009, *ApJS*, 180, 306
- Dvali, G., Gabadadze, G., & Porrati, M., 2000, *Phys. Lett. B*, 485, 208
- Eisenstein, D. J., & Hu, W., 1998, *ApJ*, 496, 605
- Enqvist, K., & Mattsson, T., 2007, *Journal of Cosmology and Astro-Particle Physics*, 2, 19
- Faber, S. M., & Gallagher, J. S., 1979, *ARAA*, 17, 135
- Fabricant, D., Lecar, M., & Gorenstein, P., 1980, *ApJ*, 241, 552
- Fang, W., & Haiman, Z., 2007, *Phys. Rev. D*, 75, 043010
- Fogli, G. L. et al., 2008, *Phys. Rev. D*, 78, 033010
- Habib, S. et al., 2009, in prep.
- Habib, S., Heitmann, K., Higdon, D., Nakhleh, C., & Williams, B., 2007, *Phys. Rev. D*, 76, 083503
- Hannestad, S., Tu, H., & Wong, Y. Y., 2006, *Journal of Cosmology and Astro-Particle Physics*, 6, 25
- Heavens, A., 2003, *MNRAS*, 343, 1327
- Heavens, A. F., Kitching, T. D., & Taylor, A. N., 2006, *MNRAS*, 373, 105
- Heavens, A. F., Kitching, T. D., & Verde, L., 2007, *MNRAS*, 380, 1029
- Heitmann, K., Higdon, D., Nakhleh, C., & Habib, S., 2006, *ApJL*, 646, L1
- Heitmann, K., Higdon, D., White, M., Habib, S., Williams, B. J., & Wagner, C., 2009, ArXiv e-prints, 0902.0429
- Heitmann, K., White, M., Wagner, C., Habib, S., & Higdon, D., 2008, ArXiv e-prints, 0812.1052
- Hu, W., & Jain, B., 2004, *Phys. Rev. D*, 70, 043009
- Huterer, D., & Linder, E. V., 2007, *Phys. Rev. D*, 75, 023519
- Huterer, D., & Takada, M., 2005, *Astroparticle Physics*, 23, 369
- Huterer, D., Takada, M., Bernstein, G., & Jain, B., 2006, *MNRAS*, 366, 101
- Ishak, M., Upadhye, A., & Spergel, D. N., 2006, *Phys. Rev. D*, 74, 043513
- Jain, B., Jarvis, M., & Bernstein, G., 2006, *Journal of Cosmology and Astro-Particle Physics*, 2, 1
- Jain, B., & Zhang, P., 2008, *Phys. Rev. D*, 78, 063503
- Jeffreys, H., 1961, *Theory of Probability*. Oxford University Press
- Jiménez, J. B., & Maroto, A. L., 2007, *Phys. Rev. D*, 76, 023003
- Jing, Y. P., Zhang, P., Lin, W. P., Gao, L., & Springel, V., 2006, *ApJL*, 640, L119
- Kia kotou, A., Elgarøy, Ø., & Lahav, O., 2008, *Phys. Rev. D*, 77, 063005
- Kitching, T. D., Heavens, A. F., Taylor, A. N., Brown, M. L., Meisenheimer, K., Wolf, C., Gray, M. E., & Bacon, D. J., 2007, *MNRAS*, 376, 771
- Kitching, T. D., Heavens, A. F., Verde, L., Serra, P., & Melchiorri, A., 2008a, *Phys. Rev. D*, 77, 103008
- Kitching, T. D., Taylor, A. N., & Heavens, A. F., 2008b, *MNRAS*, 389, 173
- Knox, L., 2006, *Phys. Rev. D*, 73, 023503
- Knox, L., Song, Y.-S., & Tyson, J. A., 2006a, *Phys. Rev. D*, 74, 023512
- Knox, L., Song, Y.-S., & Zhan, H., 2006b, *ApJ*, 652, 857
- Koivisto, T., & Mota, D. F., 2008, *Journal of Cosmology and Astro-Particle Physics*, 6, 18
- Komatsu, E. et al., 2009, *ApJS*, 180, 330
- Kunz, M., & Sapone, D., 2007, *Phys. Rev. Lett.*, 98, 121301
- Laszlo, I., & Bean, R., 2008, *Phys. Rev. D*, 77, 024048
- Linder, E. V., 2005a, *Phys. Rev. D*, 72, 043529
- , 2005b, *Astroparticle Physics*, 24, 391
- Linder, E. V., & Cahn, R. N., 2007, *Astroparticle Physics*, 28, 481
- Lue, A., Scoccimarro, R., & Starkman, G., 2004, *Phys. Rev. D*, 69, 044005
- Lukić, Z., Heitmann, K., Habib, S., Bashinsky, S., & Ricker, P. M., 2007, *ApJ*, 671, 1160
- Lukić, Z., Reed, D., Habib, S., & Heitmann, K., 2009, *ApJ*, 692, 217
- Ma, Z., Hu, W., & Huterer, D., 2006, *ApJ*, 636, 21

- Mangano, G., Melchiorri, A., Mena, O., Miele, G., & Slosar, A., 2007, *Journal of Cosmology and Astro-Particle Physics*, 3, 6
- Matarrese, S., & Verde, L., 2008, *ApJL*, 677, L77
- Nishimichi, T. et al., 2008, ArXiv e-prints, 0810.0813
- Nusser, A., Gubser, S. S., & Peebles, P. J., 2005, *Phys. Rev. D*, 71, 083505
- Oyaizu, H., 2008, *Phys. Rev. D*, 78, 123523
- Perlmutter, S. et al., 1999, *ApJ*, 517, 565
- Reed, D. S., Bower, R., Frenk, C. S., Jenkins, A., & Theuns, T., 2007, *MNRAS*, 374, 2
- Riess, A. G. et al., 1998, *AJ*, 116, 1009
- Rozo, E. et al., 2009, Astrophysics eprint, 0902.3702
- Rubin, V. C., Thonnard, N., & Ford, Jr., W. K., 1978, *ApJL*, 225, L107
- Rudd, D. H., Zentner, A. R., & Kravtsov, A. V., 2008, *ApJ*, 672, 19
- Schmidt, F., Lima, M., Oyaizu, H., & Hu, W., 2008, ArXiv e-prints, 0812.0545
- Schneider, M. D., Knox, L., Habib, S., Heitmann, K., Higdon, D., & Nakhleh, C., 2008, *Phys. Rev. D*, 78, 063529
- Seljak, U., Slosar, A., & McDonald, P., 2006, *Journal of Cosmology and Astro-Particle Physics*, 10, 14
- Simpson, F., & Bridle, S., 2005, *Phys. Rev. D*, 71, 083501
- Slosar, A., 2006, *Phys. Rev. D*, 73, 123501
- Song, Y.-S., 2005, *Phys. Rev. D*, 71, 024026
- Song, Y.-S., & Doré, O., 2008, ArXiv e-prints, 0812.0002
- Spergel, D. N. et al., 2003, *ApJS*, 148, 175
- Stabenau, H. F., & Jain, B., 2006, *Phys. Rev. D*, 74, 084007
- Stanek, R., Rudd, D., & Evrard, A. E., 2009, *MNRAS*, 394, L11
- Taylor, A. N., Kitching, T. D., Bacon, D. J., & Heavens, A. F., 2007, *MNRAS*, 374, 1377
- Tegmark, M. et al., 2004, *ApJ*, 606, 702
- Tinker, J., Kravtsov, A. V., Klypin, A., Abazajian, K., Warren, M., Yepes, G., Gottlöber, S., & Holz, D. E., 2008, *ApJ*, 688, 709
- Verde, L. et al., 2002, *MNRAS*, 335, 432
- Wang, S., Hui, L., May, M., & Haiman, Z., 2007, *Phys. Rev. D*, 76, 063503
- Wechsler, R. et al., 2009, in prep.
- White, M., 2004, *Astroparticle Physics*, 22, 211
- Zentner, A. R., Rudd, D. H., & Hu, W., 2008, *Phys. Rev. D*, 77, 043507
- Zhan, H., 2006, *Journal of Cosmology and Astro-Particle Physics*, 8, 8
- Zhan, H., & Knox, L., 2004, *ApJL*, 616, L75
- , 2006, ArXiv Astrophysics e-prints, astro-ph/0611159
- Zhan, H., Knox, L., & Tyson, J. A., 2009, *ApJ*, 690, 923
- Zhan, H., Wang, L., Pinto, P., & Tyson, J. A., 2008, *ApJL*, 675, L1
- Zhang, J., Hui, L., & Stebbins, A., 2005, *ApJ*, 635, 806
- Zhang, P., Liguori, M., Bean, R., & Dodelson, S., 2007, Physical Review Letters, 99, 141302
- Zwicky, F., 1933, *Helvetica Physica Acta*, 6, 110
- , 1937, *ApJ*, 86, 217

# A Assumed Cosmology

*Hu Zhan*

One of the most important scientific goals of the LSST is to refine and rigorously test our current “standard model” of cosmology. In predictions of LSST’s performance, however, we must agree on a fiducial cosmology, which we describe here. This book will describe our predictions for LSST’s ability to tighten our constraints on these parameters, test for consistency among a variety of cosmological probes, and test some of the basic assumptions of the model, from the Cosmological Principle, to the clustering and isotropy of dark energy.

Our fiducial model is a cold dark matter (CDM) universe with a large fraction of its energy density in the form of dark energy that has an equation of state  $w = p/\rho$  ( $w$ CDM). This model is characterized by the 11 parameters listed in [Table A.1](#), which are taken from the WMAP five-year data analysis ([Dunkley et al. 2009](#)). We use the WMAP-only results to avoid dealing with the complex correlations between LSST probes and other probes incorporated in [Dunkley et al. \(2009\)](#). Slight changes to the fiducial model do not affect our assessment of the LSST performance. Since the cosmic microwave background (CMB) alone cannot constrain all 11 parameters, we center the fiducial model on the concordance  $\Lambda$ CDM model (i.e.,  $w_0 = -1$ ,  $w_a = 0$ , and  $\Omega_k = 0$ ) and allow all the 11 parameters to float in the forecasts.

We adopt a phenomenological parametrization for the dark energy equation of state used by the report of the Dark Energy Task Force ([Albrecht et al. 2006](#)):  $w(a) = w_0 + w_a(1 - a)$ , where  $a$  is the expansion factor. The rest of the parameters are chosen to be convenient for techniques such as baryon acoustic oscillations (BAO) and weak lensing and for combining LSST constraints with CMB results. For example, the lensing potential scales with the physical matter density  $\omega_m$ , not by the matter fraction  $\Omega_m$  alone ( $\omega_m = \Omega_m h^2$  and  $h$  is the reduced Hubble constant). Likewise, the BAO features are determined by  $\omega_m$  and the physical baryon density  $\omega_b = \Omega_b h^2$ , where  $\Omega_b$  is the baryon fraction.

In addition to [Table A.1](#), we also make standard assumptions about other parameters and processes, e.g., adiabatic initial condition, standard recombination history, three effective number of neutrino species, etc. We fix the neutrino mass to zero in all but [§ 15.2](#) where we estimate the upper limit that can be placed by LSST shear and galaxy clustering data. The actual values of the neutrino masses have little impact on most forecasts, as long as they are held fixed.

## References

- Albrecht, A. et al., 2006, ArXiv Astrophysics e-prints, astro-ph/0609591  
Dunkley, J. et al., 2009, *ApJS*, 180, 306

Table A.1: Cosmological parameters from WMAP five-year results<sup>†</sup>

Symbol	Value	Remarks
$w_0$	-1	dark energy equation of state at $z = 0$
$w_a$	0	rate-of-change of the dark energy EOS as in $w(a) = w_0 + w_a(1 - a)$
$\omega_m$	0.133	physical matter density $\omega_m = \Omega_m h^2$ , $\Omega_m = 0.258$
$\omega_b$	0.0227	physical baryon density $\omega_b = \Omega_b h^2$ , $\Omega_b = 0.0441$
$\theta_s$	$0.596^\circ$	angular size of the sound horizon at the last scattering surface
$\Omega_k$	0	curvature parameter
$\tau$	0.087	optical depth to scattering by electrons in the reionized intergalactic medium
$Y_p$	0.24	primordial helium mass fraction
$n_s$	0.963	spectral index of the primordial scalar perturbation power spectrum
$\alpha_s$	0	running of the primordial scalar perturbation power spectrum
$\Delta_R^2$	$2.13 \times 10^{-9}$	normalization of the primordial curvature power spectrum at $k^* = 0.05 \text{ Mpc}^{-1}$ ( $\sigma_8 = 0.796$ or $\Delta_R^2 = 2.41 \times 10^{-9}$ at $k^* = 0.002 \text{ Mpc}^{-1}$ )

<sup>†</sup> The reduced Hubble constant  $h = 0.719$  and the present equivalent matter fraction of dark energy  $\Omega_X = 0.742$  are implicit in this parametrization, meaning that either one of them can replace  $\theta_s$  or any parameter that affects  $\theta_s$ .

# B Analysis Methods

*Phil Marshall, Licia Verde, Hu Zhan*

This chapter describes the statistical analysis methods that are used in previous chapters either to forecast LSST performance or as suggested to analyze LSST data. We start with an introductory review before moving on to some practical examples.

## B.1 Basic Parameter Estimation

Very readable introductions to probabilistic data analysis are given by [Sivia \(1996\)](#), [MacKay \(2003\)](#) and [Jaynes \(2003\)](#); an introduction to the basics is given in this section. A single piece of experimental data is often presented in the form  $x = x_0 \pm \sigma_0$ , with  $x_0$  being the result of the measurement and  $\sigma_0$  the estimate of its uncertainty. This is shorthand for something like the statement “I believe that the quantity I am trying to measure,  $x$ , is most likely from my experiments to be  $x_0$ , but I could also believe that it was actually less than or greater than this by roughly  $\sigma_0$ .” That is, the relation  $x = x_0 \pm \sigma_0$  is a compressed version of the probability distribution (or probability density function, PDF)  $\Pr(x_0|x, H)$ , to be read as the probability of getting  $x_0$  given assumptions about  $x$  and  $H$ . When written as a function of the model parameters, this PDF is referred to as the likelihood. Since our observed data come in probability distribution form, any conclusions we draw from them will necessarily be probabilistic in nature as well.

Traditionally there are two interpretations of probability: “Frequentist” and “Bayesian.” For frequentists, probabilities are just frequencies of occurrence:  $\mathcal{P} = n/N$  where  $n$  denotes the number of successes and  $N$  the total number of trials. Probability is then defined as the limit for the number of independent trials going to infinity. In the example above if one were to repeat the experiment an infinite number of times, then  $x$  will fall in the range  $[x_0 - \sigma_0, x_0 + \sigma_0]$ , say, 68% of the time. Bayesians instead interpret probability as a degree of belief in a hypothesis – a quantified version of the original statement above.

In cosmology, statistical analysis tends to be carried out in the Bayesian framework. It is easy to understand why: cosmic variance makes cosmologists only too aware of the limited information available to them. Only one realization of the CMB anisotropy and the large scale structure is accessible to our telescopes, and so while this is not a technical barrier to our happily simulating large numbers of fictitious universes in order to either compute or interpret our uncertainties, it is perhaps something of a psychological one, promoting the acceptance of the Bayesian notion of probability.

Bayesian cosmologists, seeking a steady point for their lever, assume that the observable universe is just one particular realization of a true underlying stochastic model of the Universe: the cosmological parameters of this model can be inferred from this one realization via the rules of probability.

Only if we could average all possible (unobservable) realizations of the underlying model could we recover the true values of the parameters with certainty – but since we can only observe one of the infinite possible realizations of it, we have to settle for probability distributions for the parameters of the underlying model instead.

This mental approach has the distinct advantage that it keeps cosmologists honest about the assumptions they are making, not only about the underlying world model, but also every other aspect of the data set they are attempting to model: systematic errors should, in principle, be already at the forefront of her mind! The catch is that to interpret probability as a degree of belief in an hypothesis, Bayesian cosmologists have to assume a probability distribution for the hypothesis itself. This step can be somewhat arbitrary and thus subjective: this is the age-old point of friction between frequentists and Bayesians. In this appendix we will use the Bayesian framework, in keeping with the tradition of cosmology. We will nevertheless try to point out where the “subjectivity” of being Bayesian is introduced (and where it is not).

After this aside, let us return to practicalities. The precise functional form of the likelihood is always unknown, and so an assumption must be made about it before any interpretation of the data can occur. This assumption forms part of a model for the data, which we denote by  $H$ , whilst  $x$  is a variable parameter of this model. More often than not, the physical nature of the object being studied is best understood in terms of some different parameter,  $\theta$ , rather than  $x$ : in this case the model still allows the datum  $x_0$  to be predicted, and describes how its probability is distributed through  $\Pr(x_0|\theta, H)$ . If more than one datum is available, and they came from independent attempted measurements of  $x$ , we can write the joint likelihood as

$$\Pr(x_0, x_1, x_2, \dots | \theta, H) = \Pr(x_0|\theta, H)\Pr(x_1|\theta, H)\Pr(x_2|\theta, H) \dots, \quad (\text{B.1})$$

the product rule for combining independent probabilities. This makes clearer the distinction between the parameter  $\theta$  and the data (which can be conveniently packaged into the vector  $\mathbf{d}$  having components  $x_i$ ). Indeed, a more complicated model for the data would make use of more than one parameter when predicting the data; these can be described by the parameter vector  $\boldsymbol{\theta}$ . The generalization of Equation B.1 to  $N_d$  independent data sets,  $\{\mathbf{d}_j\}$ , is then:

$$\Pr(\mathbf{d}|\boldsymbol{\theta}, H) = \prod_{j=1}^{N_d} \Pr(\mathbf{d}_j|\boldsymbol{\theta}, H). \quad (\text{B.2})$$

Within a given model then, the likelihood  $\Pr(\mathbf{d}|\boldsymbol{\theta}, H)$  can be calculated for any values of the model parameters  $\boldsymbol{\theta}$ . However, as outlined above, cosmologists want statistical inferences, i.e., we want to learn more about our model and its parameters from the data, by calculating the posterior distribution  $\Pr(\boldsymbol{\theta}|\mathbf{d}, H)$ . This distribution contains all the information about the model supplied by the data, as well as all the information we had about the model other than that provided by the data: this can be seen by applying the product rule of conditional probability to give Bayes’ theorem,

$$\Pr(\boldsymbol{\theta}|\mathbf{d}, H) = \frac{\Pr(\mathbf{d}|\boldsymbol{\theta}, H) \Pr(\boldsymbol{\theta}|H)}{\Pr(\mathbf{d}|H)}. \quad (\text{B.3})$$

The prior  $\Pr(\boldsymbol{\theta}|H)$  encodes the additional information (this is where the subjectivity of the Bayesian approach comes in), and is a PDF normalized over the parameter space. The likelihood is also a frequentist quantity (without dependence on the prior) while the posterior is a

Bayesian construct. In practical applications of Bayesian parameter inference it is good practice therefore to check how much the reported result depend on the choice of prior: reliable results depend very weakly on the prior chosen. This is in fact a form of model comparison: for Bayesians, a complete data model consists of a parameter set *and* the prior PDF for those parameters: some priors are more appropriate than others. We discuss quantitative model comparison below: in this context it provides a way of recovering some objectivity in Bayesian analysis.

## B.2 Assigning and Interpreting PDFs

As [Equation B.3](#) shows, computing the probability distribution for a parameter (and hence measuring it) necessarily involves the assignment of a prior PDF for that parameter. There are two types of prior we can assign:

- **Uninformative priors**, such as uniform distributions in the parameter or its logarithm (the Jeffreys prior) are often assumed. Sometimes we genuinely know very little, and so minimizing the average information content of a prior PDF (or maximizing its entropy) makes sense. In other situations we do know something about a model parameter, but choose to assign an uninformative prior in order to investigate cleanly the information content of the data. Sometimes the reason given is to “give an unbiased result.” This makes less sense, given that Bayesian inferences are biased by design – biased towards what is already known about the system.
- **Informative priors**: it is very rare to know *nothing* about a model and its parameters. An experiment has usually been carried out before, with different data! The best kind of prior PDF is the posterior PDF of a previous experiment – this is exactly equivalent to combining data sets in a joint analysis ([Equation B.2](#) above).

Given suitably assigned priors and likelihoods then, the posterior distribution gives the probability of the parameter vector lying between  $\boldsymbol{\theta}$  and  $(\boldsymbol{\theta} + d\boldsymbol{\theta})$ . This is the answer to the problem, the complete inference within the framework of the model. However, we typically need to present some compressed version of the posterior PDF: what should we do?

The probability distribution for a single parameter  $\theta_N$  is given by marginalization over the other parameters,

$$\Pr(\theta_N|\mathbf{d}, H) = \int \Pr(\boldsymbol{\theta}|\mathbf{d}, H) d^{N-1}\boldsymbol{\theta}. \quad (\text{B.4})$$

This is the addition rule for probabilities, extended to the continuous variable case<sup>1</sup>. This single parameter, one-dimensional marginalized posterior is most useful when the parameter is the only one of interest. In other cases we need to represent the posterior PDF and the parameter constraints that it describes in higher dimensions – although beyond two dimensions the posterior PDF becomes very difficult to plot.

The one-dimensional marginalized posterior PDFs can be further compressed into their means, or medians, or confidence intervals containing some fraction of the total probability – confidence

<sup>1</sup>Sometimes [Equation B.4](#) is used with the posterior  $\Pr(\boldsymbol{\theta}|\mathbf{d}, H)$  substituted by the likelihood. Even in this case a Bayesian step has been taken: a uniform prior is “hidden” in the parameter space “measure”  $d^{N-1}\boldsymbol{\theta}$ .

intervals need to be defined carefully as the integrals can be performed a number of different ways. However, note that the set of one-dimensional marginalized posterior means (or medians, etc.) need not itself represent a model that is a good fit to the data. The “best-fit” point is the position in parameter space where the likelihood function has a global maximum. This point is of most interest when the prior PDF is uninformative: in the case of uniform prior PDFs on all parameters, the peak of the likelihood coincides with the peak of the posterior PDF, but in general it does not. Moreover, the maximum likelihood model is necessarily the model most affected by the noise in the data – if any model “over-fits” the data, it is that one! Graphical displays of marginalized posterior PDFs remain the most complete way to present inferences; propagating the full posterior PDF provides the most robust estimates of individual parameters.

One class of parameters that are invariably marginalized over in the final analysis are the so-called nuisance parameters. The model  $H$  is a model for the data, not just the physical system of interest: often there are aspects of the experimental setup that are poorly understood, and so best included in the model as functions with free parameters with estimated prior PDFs. This procedure allows the uncertainty to be propagated into the posterior PDF for the interesting parameters. Examples of nuisance parameters might include: calibration factors, unknown noise or background levels, point spread function widths, window function shapes, supernova dust extinctions, weak lensing mean source redshifts, and so on. If a systematic error in an experiment is identified, parametrized and then that nuisance parameter marginalized over, then it can be said to have been translated into a statistical error (seen as a posterior PDF width): a not unreasonable goal is to translate all systematic errors into statistical ones.

### B.3 Model Selection

While the goal of parameter estimation is to determine the posterior PDF for a model’s parameters, perhaps characterized simply by the most probable or best-fit values and their errors, model selection seeks to distinguish between different models, which in general will have different sets of parameters. Simplest is the case of *nested* models, where the more complicated model has additional parameters, in addition to those in the simpler model. The simpler model may be interpreted as a particular case for the more complex model, where the additional parameters are kept fixed at some fiducial values. The additional parameters may be an indication of new physics, thus the question one may ask is: “would the experiment provide data with enough statistical power to require additional parameters and therefore to signal the presence of new physics if the new physics is actually the true underlying model?” Examples of this type of question are: “do the observations require a modification to general relativity as well as a universe dominated by dark energy?” (§ 15.3), or, “do the observations require a new species of neutrino?” (§ 15.2). However, completely disparate models, with entirely different parameter sets can also be compared using the Evidence ratio. In this case, it is even more important to assign realistic and meaningful prior PDFs to all parameters.

These questions may be answered in a Bayesian context by considering the Bayesian Evidence ratio, or Bayes factor,  $B$ :

$$B = \frac{\Pr(\mathbf{d}|H_1)}{\Pr(\mathbf{d}|H_2)}, \tag{B.5}$$

where  $H_1$  and  $H_2$  represent the two models being compared. The Bayes factor is related to the perhaps more desirable posterior ratio

$$\frac{\Pr(H_1|\mathbf{d})}{\Pr(H_2|\mathbf{d})} = \frac{\Pr(\mathbf{d}|H_1)}{\Pr(\mathbf{d}|H_2)} \frac{\Pr(H_1)}{\Pr(H_2)}. \quad (\text{B.6})$$

by the ratio of model prior probabilities. The latter is not, in general straightforward to assign with differences of opinion between analysts common. However, the Bayes factor itself can be calculated objectively once  $H_1$  and  $H_2$  have been defined, and so is the more useful quantity to present.

If there is no reason to prefer one hypothesis over another other than that provided by the data, the ratio of the probabilities of each of the two models being true is just given by the ratio of evidences. Another way of interpreting a value of  $B$  greater than unity is as follows: if models  $H_1$  and  $H_2$  are still to be presented as equally probable after the experiment has been performed, then proponents of the lower-evidence model  $H_2$  must be willing to offer odds of  $B$  to one against  $H_1$ . In practice, the Bayesian Evidence ratio can be used simply to say that “the probability of getting the data would be  $B$  times higher if model  $H_2$  were true than if  $H_2$  were.” Indeed, [Jeffreys \(1961\)](#) proposed that  $1 < \ln B < 2.5$  be considered as “substantial” evidence in favor of a model,  $2.5 < \ln B < 5$  as “strong,” and  $\ln B > 5$  as “decisive.” Other authors have introduced different terminology (e.g., [Trotta 2007a](#)).

The evidence  $\Pr(\mathbf{d}|H)$  is the normalization of the posterior PDF for the parameters, and so is given by integrating the product of the likelihood and the prior over all  $N$  parameters:

$$\Pr(\mathbf{d}|H) = \int \Pr(\mathbf{d}|\boldsymbol{\theta}, H) \Pr(\boldsymbol{\theta}|H) d^N \boldsymbol{\theta}. \quad (\text{B.7})$$

There is ample literature on applications of Bayesian Evidence ratios in cosmology (e.g. [Jaffe 1996](#); [Hobson et al. 2002](#); [Saini et al. 2004](#); [Liddle et al. 2006](#); [Marshall et al. 2006](#); [Parkinson et al. 2006](#); [Mukherjee et al. 2006a](#); [Pahud et al. 2006](#); [Szydlowski & Godlowski 2006b,a](#); [Trotta 2007b](#); [Pahud et al. 2007](#)). The evidence calculation typically involves computationally expensive integration [Skilling \(2004\)](#); [Trotta \(2007a\)](#); [Beltrán et al. \(2005\)](#); [Mukherjee et al. \(2006a,b\)](#); [Parkinson et al. \(2006\)](#); however, it can often be approximated just as the model parameter posterior PDF can. For example, [Heavens et al. \(2007\)](#) shows how, by making simplifying assumptions in the same spirit of Fisher’s analysis ([Fisher 1935](#)), one can compute the expected evidence for a given experiment, in advance of taking any data, and forecast the extent to which an experiment may be able to distinguish between different models. We implement this in § 15.2 and § 15.3. In § 15.2 we consider the issue of deviations from the standard number of three neutrino species. The simplest model has three neutrino species, but effectively this number can be changed by the existence of a light particle that does not couple to electrons, ions or photons, or by the decay of dark matter particles, or indeed any additional relativistic particle. Given the observables and errors achievable from a survey with given specifications, we use the evidence in order to address the issue of how much different from the standard value the number of neutrino species should be such that the alternative model should be favored over the reference model.

In § 15.3 we also employ the Bayesian evidence: this time the reference model is a cold dark matter + dark energy model, where gravity is described by General Relativity (GR). In the alternative model, GR is modified so that the growth of cosmological structure is different. Again, given the

observables and errors achievable from a survey with given specifications, we use the evidence to quantify how different from the GR prediction the growth of structure would have to be such that the alternative model should be preferred.

## B.4 PDF Characterization

The conceptually most straightforward way to carry out parameter inference (and model selection) is to tabulate the posterior PDF  $\Pr(\boldsymbol{\theta}|\mathbf{d}, H)$  on a suitable grid, and normalize it via simple numerical integration. This approach is unlikely to be practical unless the number of parameters is very small and the PDF is very smooth. The number of function evaluations required increases exponentially with the dimensionality of the parameter space; moreover, the following marginalization integrals will all be correspondingly time-consuming. In this section we consider two more convenient ways to characterize the posterior PDF — the multivariate Gaussian (or Laplace) approximation, and Markov Chain Monte Carlo sampling.

### B.4.1 The Laplace Approximation

By the central limit theorem, the product of a set of convex functions tends to the Gaussian functional form in the limit of large set size (Jaynes 2003); the posterior probability distribution of Equation B.3 often fits this bill, suggesting that the Gaussian distribution is likely to be a good approximation to the posterior density. Approximating probability distributions with Gaussians is often referred to as the Laplace approximation (see e.g. Sivia 1996; MacKay 2003).

In one dimension, a suitable Gaussian can be found by Taylor expansion about the peak position  $\theta_0$  of the logarithm of the posterior PDF  $P(\theta)$  (where the conditioning on the data and the model have been dropped for clarity):

$$\log P(\theta) \approx \log P(\theta_0) + \frac{1}{2}(\theta - \theta_0)^2 \frac{d^2 P}{d\theta^2} \Big|_{\theta_0}. \quad (\text{B.8})$$

Exponentiating this expression gives the Gaussian approximation to the function,

$$g(\theta) \approx P(\theta_0) \exp \left[ -\frac{(\theta - \theta_0)^2}{2\sigma^2} \right]. \quad (\text{B.9})$$

The width  $\sigma$  of this Gaussian satisfies the following relation:

$$\frac{d^2 \log P}{d\theta^2} \Big|_{\theta_0} = -\frac{1}{\sigma^2}. \quad (\text{B.10})$$

The extension of this procedure to multivariate distributions is straightforward: instead of a single variance  $\sigma^2$ , an  $N \times N$  covariance matrix  $\mathbf{C}$  is required, such that the posterior approximation is

$$g(\boldsymbol{\theta}) = P(\boldsymbol{\theta}_0) \exp \left[ -\frac{1}{2}(\boldsymbol{\theta} - \boldsymbol{\theta}_0)^T \mathbf{C}^{-1}(\boldsymbol{\theta} - \boldsymbol{\theta}_0) \right], \quad (\text{B.11})$$

and the covariance matrix has components

$$(\mathbf{C}^{-1})_{ij} = -\frac{\partial^2 \log P}{\partial \theta_i \partial \theta_j} \Big|_{\boldsymbol{\theta}_0}. \quad (\text{B.12})$$

(This matrix is very unlikely to be diagonal – correlations, or degeneracies, between parameters are encoded in its off-diagonal elements.) The problem is now reduced to finding (numerically) the peak of the log-posterior, and its second derivatives at that point. When the data quality is good, one may expect the individual datum likelihoods to be already quite convex, giving a very peaky unimodal posterior: in this case the Gaussian approximation is likely to be both accurate, and more quickly and easily located. More commonly, techniques such as simulated annealing may be necessary when finding the maximum of complex functions of many parameters; in this case a Gaussian may not be such a good approximation anyway.

### B.4.2 Fisher Matrices

The Fisher information matrix (Fisher 1935) is widely used for forecasting survey performance and for identifying dominant systematic effects (see e.g., Albrecht et al. 2009). The Fisher matrix formalism is very closely related to the Laplace approximation to the parameter posterior described above. The discussion that follows may seem unconventional to those more familiar with its frequentist origins and presentation: our aim is to show how the formalism has been adapted to modern Bayesian cosmology.

The Fisher matrix was originally defined to be

$$F_{\alpha\beta} = -\left\langle \frac{\partial^2 \ln P(\mathbf{x}|\mathbf{q})}{\partial q_\alpha \partial q_\beta} \right\rangle, \quad (\text{B.13})$$

where  $\mathbf{x}$  is a data vector,  $\mathbf{q}$  is the vector of model parameters, and  $\langle \dots \rangle$  denotes an ensemble average. If the prior PDFs are non-uniform, we must replace the likelihood  $P(\mathbf{x}|\mathbf{q})$  by the posterior  $P(\mathbf{q}|\mathbf{x})$ . In any case, we recognize the Laplace approximation and identify (by comparison with Equation B.12) the ensemble average covariance matrix of the inferred parameters as  $\mathbf{F}^{-1}$ .

This estimate of the forecast parameter uncertainties really corresponds to the best case scenario, as dictated by the Cramer-Rao theorem. More specifically, the estimated error of the parameter  $q_\alpha$  is  $\sigma(q_\alpha) \geq (F_{\alpha\alpha})^{-1/2}$  if all other parameters are known precisely, or  $\sigma(q_\alpha) \geq [(\mathbf{F}^{-1})_{\alpha\alpha}]^{1/2}$  if all the parameters are estimated from the data.

Cosmological applications of the Fisher matrix were introduced by Jungman et al. (1996); Vogeley & Szalay (1996); Tegmark et al. (1997); Tegmark (1997). The key is to identify the correct likelihood function  $P(\mathbf{x}|\mathbf{q})$  (which is anyway crucial for all inference techniques). However, the Fisher matrix analysis has a further limitation due to the Gaussian approximation of  $P(\mathbf{q}|\mathbf{x})$  with respect to  $\mathbf{q}$ : the likelihood, priors and indeed choice of parametrization need to be such that this approximation is a good one. Usual practice is to approximate the likelihood function as Gaussian, and assert either Gaussian or uniform priors (both of which guarantee the Gaussianity of the posterior PDF).

If we approximate the likelihood function by a Gaussian distribution then,

$$P(\mathbf{x}|\mathbf{q}) = \frac{1}{(2\pi)^{N/2} \det[\mathbf{C}(\mathbf{q})]} \exp \left\{ [\mathbf{x} - \bar{\mathbf{x}}(\mathbf{q})]^T \frac{\mathbf{C}^{-1}(\mathbf{q})}{2} [\mathbf{x} - \bar{\mathbf{x}}(\mathbf{q})] \right\}, \quad (\text{B.14})$$

where  $N$  is the dimension of the observables  $\mathbf{x}$ ,  $\bar{\mathbf{x}}(\mathbf{q})$  is the ensemble average of  $\mathbf{x}$ ,  $\mathbf{C}(\mathbf{q}) = \langle (\mathbf{x} - \bar{\mathbf{x}})(\mathbf{x} - \bar{\mathbf{x}})^T \rangle$  is the covariance of  $\mathbf{x}$ . The Fisher matrix is then (Tegmark et al. 1997)

$$F_{\alpha\beta} = \frac{1}{2} \text{Tr} \left( \mathbf{C}^{-1} \frac{\partial \mathbf{C}}{\partial q_\alpha} \mathbf{C}^{-1} \frac{\partial \mathbf{C}}{\partial q_\beta} \right) + \frac{\partial \bar{\mathbf{x}}}{\partial q_\alpha} \mathbf{C}^{-1} \frac{\partial \bar{\mathbf{x}}}{\partial q_\beta}, \quad (\text{B.15})$$

where we have dropped the variables  $\mathbf{q}$  in  $\mathbf{C}$  and  $\bar{\mathbf{x}}$  for clarity. To avoid confusion, we note that  $\mathbf{C}$  is the covariance matrix of the data  $\mathbf{x}$ , whereas  $\mathbf{F}^{-1}$  is the covariance matrix of the parameters  $\mathbf{q}$ .

In the Gaussian approximation, marginalization, and moment-calculating integrals are analytic. Independent Fisher matrices are additive; a Gaussian prior on  $q_\alpha$ ,  $\sigma_P(q_\alpha)$ , can be introduced via  $F_{\alpha\alpha}^{\text{new}} = F_{\alpha\alpha} + \sigma_P^{-2}(q_\alpha)$ . A Fisher matrix of the parameters  $\mathbf{q}$  can be projected onto a new set of parameters  $\mathbf{p}$  via

$$F_{\mu\nu}^{\text{new}} = \sum_{\alpha,\beta} \frac{\partial q_\alpha}{\partial p_\mu} F_{\alpha\beta} \frac{\partial q_\beta}{\partial p_\nu}. \quad (\text{B.16})$$

Fixing a parameter is equivalent to striking out its corresponding row and column in the Fisher matrix. To obtain a new Fisher matrix after marginalizing over a parameter, one can strike out the parameter's corresponding row and column in the original covariance matrix (i.e., the inverse of the original Fisher matrix) and then invert the resulting covariance matrix<sup>2</sup>.

### B.4.3 Examples

At this point, we give two worked examples from observational cosmology, describing the data model and Fisher matrix forecasts of parameter uncertainties.

#### Example 1: Type Ia Supernovae

For SNe, the observables are their peak magnitudes in a certain band

$$m_i = \bar{m}(\mathbf{q}, z_i) + n_i, \quad (\text{B.17})$$

where the subscript  $i$  labels each SN,  $\bar{m}$  is the mean value of the SN peak magnitude at redshift  $z_i$ , the parameters  $\mathbf{q}$  include both cosmological and nuisance parameters, and  $n_i$  represents the observational noise and intrinsic scatter of the peak magnitude. The mean peak magnitude is given by

$$\bar{m}_i = M + 5 \log [D_L(w_0, w_a, \Omega_m, \Omega_k, h, \dots, z)] + \text{evolution terms} + \text{const}, \quad (\text{B.18})$$

where  $M^3$  is the mean absolute peak magnitude at  $z = 0$ ,  $D_L$  is the luminosity distance, and the evolution terms account for a possible drift of the mean absolute peak magnitude with time. In a number of forecasts, the evolution terms are simply model with a quadratic function  $az + bz^2$  (e.g., Albrecht et al. 2006; Knox et al. 2006; Zhan et al. 2008).

<sup>2</sup>For a better numerical treatment, see Albrecht et al. (2009).

<sup>3</sup> $M$  is degenerate with the Hubble constant.